Wiley
Structural Control and Health Monitoring
Volume 2024, Article ID 7104844, 26 pages
https://doi.org/10.1155/2024/7104844

WILEY

Research Article

Input Energy Reduction-Oriented Control and Analytical Design of Inerter-Enabled Isolators for Large-Span Structures

Jianfei Kang[1] **Zhipeng Zhao**[2] **Yixian Li,**[3] **Liyu Xie,**[2] **and Songtao Xue**[2,4]

[1] *School of Civil Engineering, Suzhou University of Science and Technology, Suzhou 215011, China*
[2] *Department of Disaster Mitigation for Structures, Tongji University, Shanghai 200092, China*
[3] *Department of Civil and Environmental Engineering, The Hong Kong Polytechnic University, Hung Hom, Hong Kong*
[4] *Department of Architecture, Tohoku Institute of Technology, Sendai 982-8577, Japan*

Correspondence should be addressed to Zhipeng Zhao; zhaozhipeng@tongji.edu.cn

Received 2 May 2024; Accepted 3 September 2024

Academic Editor: Sara Casciati

Seismic isolation technologies for large-span structures have rapidly developed alongside the popularization of the seismic resilience concept. To produce a high-efficiency isolation technology with lower energy dissipation demands, this paper proposes a novel inerter-enabled isolator (IeI) and a tailored input energy reduction-oriented design method. The inerter-based damper within the IeI is developed by combining the dashpot, tuning spring, and two inerters to facilitate the optimization of inerter distribution. Assuming the large-span structure remains linear, the overall seismic input energy of the large-span structure with IeIs and its allocation in the superstructure and additional damping are quantified using stochastic energy analysis. The advantages of the IeI over the conventional linear viscous damper (LVD) isolator are elucidated through dimensionless parametric analysis. Based on the results of parametric analysis, an input energy reduction-oriented design method is proposed for the IeI, along with an easy-to-follow diagram that helps with preliminary design in practical applications. The effectiveness of the IeI and the proposed design method is validated through a design case study of a benchmark large-span structure. The results demonstrate that the IeI reduces the seismic response of large-span structures by simultaneously employing the input energy reduction effect of grounded inerters with the damping-enhancing effect of inerter-based dampers. The proposed design method effectively balances the performance of controlling the large-span structure and the isolator displacement. Under consistent control performance and isolator displacement constraints, the IeI requires much less damping coefficient and energy dissipation capacity than the conventional LVD isolator. Moreover, leveraging the damping enhancement and input energy reduction effects, the IeI achieves comparable control performance to the conventional LVD isolator, even under stricter isolator displacement constraints.

1. Introduction

Large-span structures provide expansive spaces of great importance for integrated commercial, transportation, and multifunctional purposes, thanks to their efficient large-spanning capability without the need for intermediate support. During the past century, the rapid development of computer-aided design has fueled the extensive use of large-span structures in engineering practice [1]. These structures, emblematic of cutting-edge design concepts and construction expertise, are frequently employed as iconic architectural landmarks, as exemplified by the Teshima Art Museum in Japan and the Water Cube in China. Although well-designed large-span structures excel in propagating and resisting vertical static gravity loads, they present challenges in efficiently withstanding horizontal dynamic loads, such as earthquake ground motion. As reported, large-span structures have experienced structural and nonstructural damage during seismic events [2–6]. Examples include the 1995 Kobe earthquake [2, 3], which caused truss members to detach from the large-span roof of the Hanshin Horse Racecourse. The 2008 Wenchuan earthquake [4] resulted in large-span structure displacements exceeding design limits, leading to the fracture and buckling of the supports. The 2016 Ya'an earthquake [6] significantly damaged numerous large-span structures, with the Lushan Middle School

Gymnasium ultimately dismantled due to irreparable permanent displacements, member fractures, and connection dislocations. The lessons from seismic damage to large-span structures and their significance as architectural landmarks and postearthquake refuges [7] have prompted scholars to emphasize seismic response analysis and control methods for these structures [8–10].

Ishikawa and Kato [11] studied the dynamic buckling collapse of reticular domes subjected to vertical ground motion, presenting an estimation formula for the maximum collapse acceleration based on domes' equivalent linear elastic responses. Kato et al. [12] highlighted that large-span structures with specific aspect ratios exhibit significant vertical displacements when subjected to horizontal seismic excitations. Takeuchi et al. [13] examined the amplification effect of the substructure on the response of large-span roofs and proposed a simplified calculation method based on amplification factors. Through shaking table tests, Nie et al. [14–16] examined the failure modes of different large-span structures, highlighting the direct relationship between the collapse and the horizontal and vertical displacements of structures.

However, a growing number of vibration control methods for large-span structures have emerged [17–20], including viscous dampers, buckling-restrained braces, bidirectional tuned mass dampers, spatially distributed tuned mass dampers, and isolation systems. In particular, as seismic resilience gains traction, isolation technology [21–25] has been widely employed for large-span structures, offering advantages in restoring postearthquake functionality. The demand for high-performance isolation devices is high, especially in cases where limited installation space is available for large-span roofs. Yong-Chul et al. [26] implemented the friction pendulum system (FPS) for isolating lattice shell domes. They suggested a certain range of the friction coefficient and radius to enhance isolation ability and simultaneously improve the energy dissipation efficiency of the FPS. By integrating the FPS with vertical air springs, Han et al. [27] proposed a three-dimensional isolation bearing, enabling efficient energy dissipation in both horizontal and vertical directions. Xu et al. [28] validated the efficacy of the isolator, comprising a viscoelastic core bearing and two viscoelastic dampers for response control in a large-span grid structure. Casciati [29] evaluated the seismic efficiency of various structural skeleton designs for base-isolated domes.

Additionally, to address the rising demand for seismic resilience, researchers are exploring the integration of a novel mechanical element, the inerter, with isolation technology to enhance seismic control performance [30–32]. The inerter, initially proposed by Kawamata and realized using a hydraulic pump to modify the inertial characteristics of buildings [33], is a mechanical element that exhibits a force output ideally proportional to the relative accelerations across its two terminals [34]. The inerter can be realized using diverse physical mechanisms [35–39], achieving significant apparent mass with minimal physical mass. With further research advancements, integrating the inerter with other mechanical elements, such as springs, dampers, and suspended masses, to achieve enhanced control performance has gained widespread acceptance [40–48]. Inerter-based dampers are characterized by their damping-enhancing effect [49, 50] and input energy reduction capacity [51]. As an improvement upon the seismic isolation device, a series of inerter-based dampers were introduced to form a hybrid isolation system [52–57]. The elongation of the period and efficient reduction in seismic response have been confirmed through the use of a force-restricted rotational viscous mass damper modeled as a complex-valued stiffness model [52]. It has been confirmed that the incorporation of tuned mass damper inerter (a commonly used type of inerter-based dampers) into seismic isolation devices provides dual benefits, including improved control performance and reduced requirements for isolator displacement [53, 54, 58]. Based on a closed-form displacement demand equation, a displacement mitigation-oriented design procedure for the inerter element-involved isolation system has been proposed in [55]. However, the studies mentioned above are limited to applying the typical inerter-based dampers to simple isolated building structures and employing primary topology forms. The applicability of the inerter-enabled isolator (IeI) in large-span structures and the suitable topology forms for such applications still need to be determined. In particular, considering the rapid construction of large-span structures with high-level seismic energy dissipation burdens, the input energy reduction benefits should be properly designed and used with priority.

This study proposes an IeI containing grounded inerter to mitigate the seismic response of large-span structures. First, the components of the IeI and corresponding governing equations are detailed. The force-displacement relationship of the IeI is validated through finite element analysis and experiments. Then, the intrinsic effect of the IeI in reducing the total input energy of the large-span structure is discovered. Subsequently, the energy and isolator displacement performance indexes are defined through stochastic energy analysis. An input energy reduction-oriented design method has been proposed based on the insights gained from parametric analysis. Finally, the proposed design method is validated using a benchmark large-span structure.

2. Inerter-Enabled Isolator

To elucidate the potential advantages and working mechanism of the IeI, this section provides a detailed description of the mechanical model for the proposed IeI and validates its force-displacement relationship through finite element analysis and experiments. The governing equations for the large-span structures with and without IeIs are established. The design approach focused on input energy reduction for the IeI will be presented in the following section.

2.1. Mechanical Model of the IeI. Figure 1(a) illustrates the mechanical model of the IeI, which combines conventional isolation techniques with an inerter-based damper. In particular, the isolating bearing is depicted as a linear spring with a horizontal stiffness coefficient, k_{iso}, and it has sufficient vertical resisting capacity to support the isolated large-span structures. Additionally, the inerter-based damper, which includes a dashpot with a damping coefficient c_{iso}, a tuning spring with a stiffness coefficient k_{t}, and two inerter elements with apparent masses $m_{\mathrm{d},1}$ and $m_{\mathrm{d},2}$, is employed to adjust the isolating frequency, dissipate vibration energy, and efficiently reduce input vibration energy. Following the enhanced energy dissipation mechanism, the dashpot, in conjunction with the inerter and spring, can produce deformations (x_{C}-x_{A}), which are greater than the displacement of the isolation layer (x_{B}-x_{A}) as shown in Figure 1(b). Here, x_{A}, x_{B}, and x_{C} denote the displacements relative to the ground of the two terminals and the middle node of the IeI, respectively.

In this condition, the corresponding resisting forces P_{A}, P_{B}, and P_{C} can be expressed as follows:

$$\begin{cases} P_{\mathrm{A}} = -k_{\mathrm{iso}}\left(x_{\mathrm{B}} - x_{\mathrm{A}}\right) - c_{\mathrm{iso}}\left(\dot{x}_{\mathrm{C}} - \dot{x}_{\mathrm{A}}\right) - m_{\mathrm{d},2}\left(\ddot{x}_{\mathrm{C}} - \ddot{x}_{\mathrm{A}}\right), \\ P_{\mathrm{B}} = k_{\mathrm{iso}}\left(x_{\mathrm{B}} - x_{\mathrm{A}}\right) + k_{\mathrm{t}}\left(x_{\mathrm{B}} - x_{\mathrm{C}}\right) + m_{\mathrm{d},1}\left(\ddot{x}_{\mathrm{B}} - \ddot{x}_{\mathrm{C}}\right), \\ P_{\mathrm{C}} = c_{\mathrm{iso}}\left(\dot{x}_{\mathrm{C}} - \dot{x}_{\mathrm{A}}\right) + m_{\mathrm{d},2}\left(\ddot{x}_{\mathrm{C}} - \ddot{x}_{\mathrm{A}}\right) - k_{\mathrm{t}}\left(x_{\mathrm{B}} - x_{\mathrm{C}}\right) - m_{\mathrm{d},1}\left(\ddot{x}_{\mathrm{B}} - \ddot{x}_{\mathrm{C}}\right). \end{cases} \tag{1}$$

Note that the external node A is grounded ($x_{\mathrm{A}} = 0$) and node C, being an internal node, is not subjected to any external forces ($P_{\mathrm{C}} = 0$). Thus, motion equation (1) can be simplified as follows:

$$\begin{Bmatrix} F_{\mathrm{IeI}} \\ 0 \end{Bmatrix} = \begin{bmatrix} m_{\mathrm{d},1} & -m_{\mathrm{d},1} \\ -m_{\mathrm{d},1} & m_{\mathrm{d},1} + m_{\mathrm{d},2} \end{bmatrix} \begin{Bmatrix} \ddot{x}_{\mathrm{B}} \\ \ddot{x}_{\mathrm{C}} \end{Bmatrix} + \begin{bmatrix} 0 & 0 \\ 0 & c_{\mathrm{iso}} \end{bmatrix} \begin{Bmatrix} \dot{x}_{\mathrm{B}} \\ \dot{x}_{\mathrm{C}} \end{Bmatrix} + \begin{bmatrix} k_{\mathrm{iso}} + k_{\mathrm{t}} & -k_{\mathrm{t}} \\ -k_{\mathrm{t}} & k_{\mathrm{t}} \end{bmatrix} \begin{Bmatrix} x_{\mathrm{B}} \\ x_{\mathrm{C}} \end{Bmatrix}, \tag{2}$$

where F_{IeI} is the output force corresponding to IeI; $F_{\mathrm{IeI}} = P_{\mathrm{B}} = -P_{\mathrm{A}}$.

2.2. Finite Element Analysis and Experimental Validation of the IeI. To investigate the practical working performance of the IeI, the accuracy of its mechanical model, as described in Section 2.1, is validated through finite element analysis and dynamic tests. As illustrated in Figure 2(a), the finite element model of the IeI is constructed in OpenSees. The spring components (elements 1 and 4) and the dashpot component (element 2) are simulated using "Twonodelink" elements, whereas the inerter components (elements 3 and 5) are modeled with specialized inerter elements, as described in Appendix A. The "Twonodelink" elements for the springs use an "Elastic" material, whereas the "Twonodelink" element for the dashpot employs a "Viscous" material. Parameters such as $m_{\mathrm{d},1}$ and $m_{\mathrm{d},2}$, both at 25.5 kg; k_{iso} and k_{t} at 6535.4 N/m and 1579.2 N/m, respectively; and c_{iso} at 31.7 N·s/m, are considered. The hysteresis curves for the parallel combined inerter and dashpot components (elements 2 and 3), as well as the overall IeI depicted in Figure 2(b), are obtained under a harmonic excitation of 15 mm amplitude at a frequency of $f = 0.8$ Hz at point B. These curves demonstrate the expected negative stiffness effect from the inerter. Moreover, the well-designed IeI amplifies the stroke of the dashpot component, achieving a larger internal damping stroke (x_C-$x_A = 44.05$ mm) with a smaller base displacement (x_B-$x_A = 15.00$ mm). This suggests that the IeI has the potential to dissipate more energy with minimal base displacement.

Experimental validation involves dynamic loading tests on the IeI's parallel combined inerter and dashpot components. The experimental setup is detailed in Figures 3(a) and 3(b). These tests are conducted using a SANF3A55/45(200) type servo actuator for harmonic loading, with force and displacement sensors monitoring the outputs of the parallel combined inerter and dashpot components. In these experiments, the inerter operates with two flywheels driven by a ball screw mechanism, while the dashpot's damping effect is achieved through eddy current damping produced by the interaction between permanent magnets and a conductor disk. The ball screw has a lead of 80 mm and a radius of 10 mm. The two flywheels consist of an iron magnet disk with a diameter of 180 mm and a thickness of 1 mm and an aluminum conductor disk with a diameter of 180 mm and a thickness of 7 mm. Six pairs of neodymium-iron-boron cylindrical magnets, each with a radius of 12.5 mm and a mass of 2.0 g, uniformly distributed along the circumference of the magnet disk with a diameter of 150 mm, are used to provide a constant magnetic field. The test results, displayed in Figures 3(c) and 3(d) with loading amplitudes of 15 mm at frequencies of $f = 1$ Hz and $f = 3$ Hz, respectively, indicate that the device's apparent mass is measured at 25.5 kg. These outcomes confirm that the theoretical model can accurately simulate the IeI.

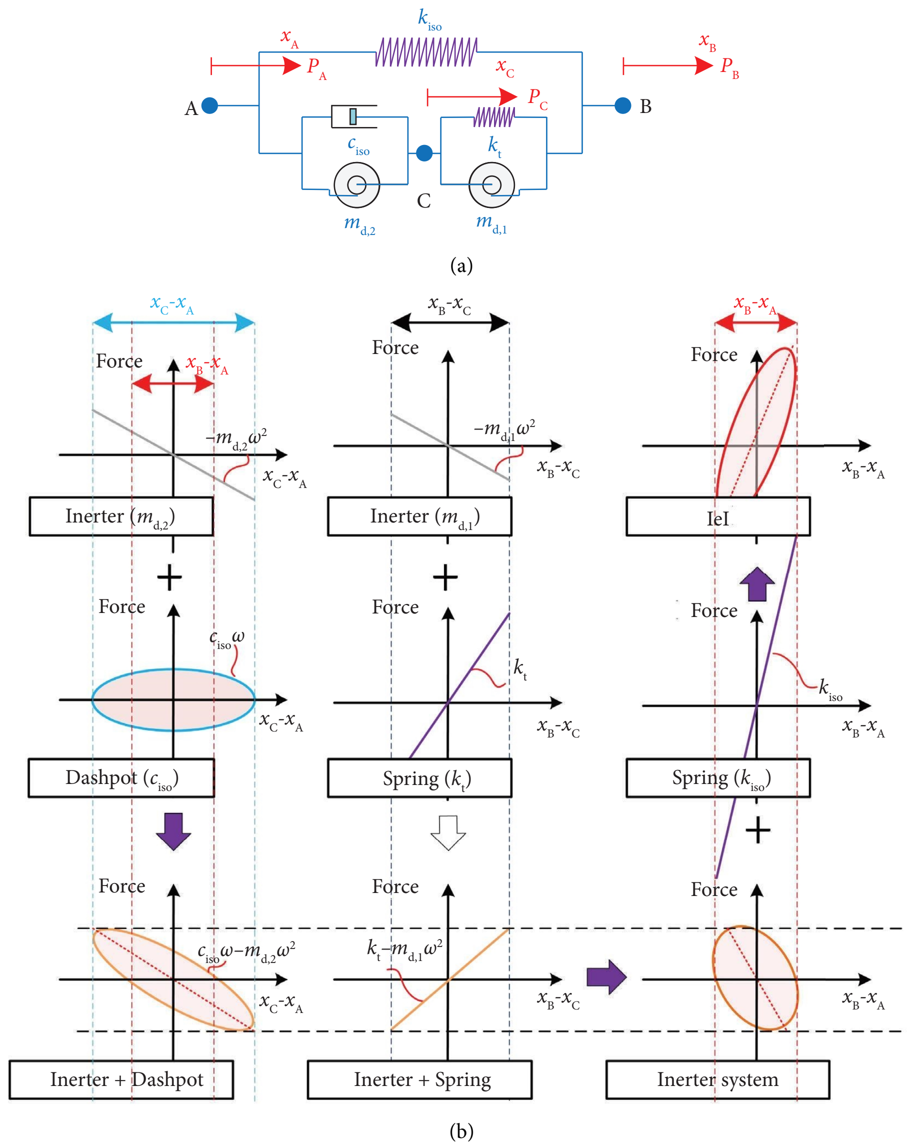

Figure 1: Mechanical model of the inerter-enabled isolator (IeI): (a) schematic model; (b) schematic representation of the hysteretic curves.

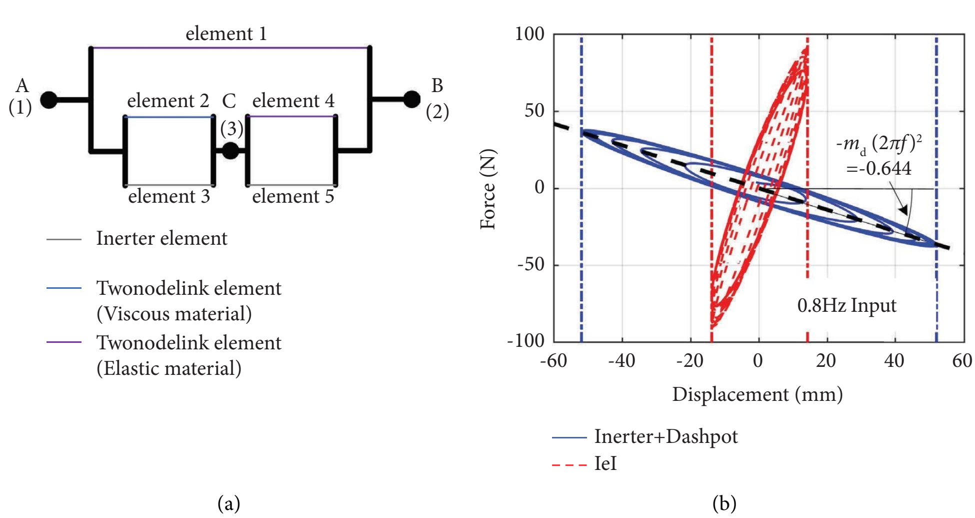

Figure 2: Finite element model and force-displacement relationship of the IeI: (a) finite element model; (b) hysteresis curves obtained through finite element analysis.

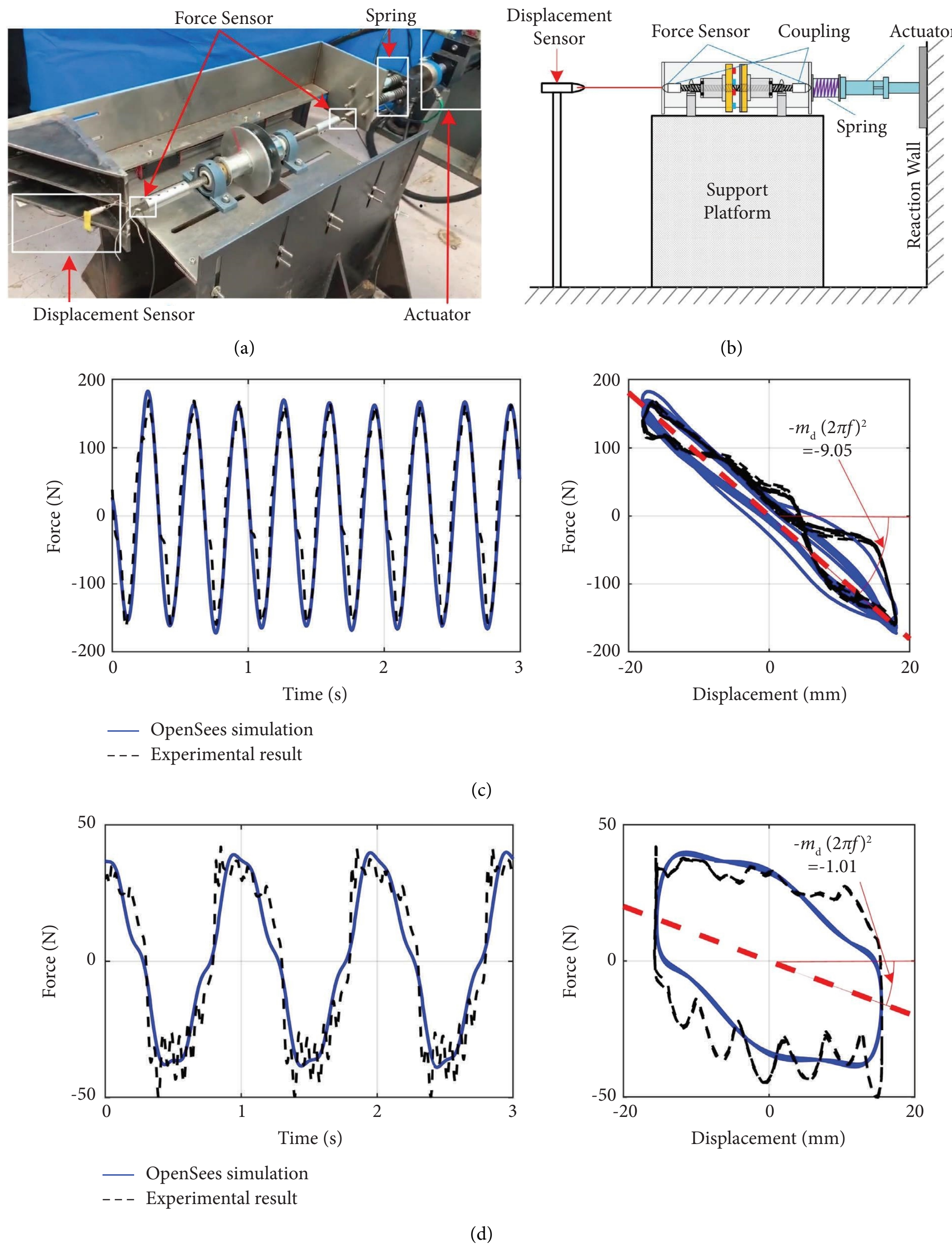

Figure 3: Experimental validation of the IeI: (a) experimental photo; (b) setup of the experiment; (c) force responses of the inerter-based damper part (1 Hz, 15 mm); (d) force responses of the inerter-based damper part (3 Hz, 15 mm).

2.3. Mechanical Model of the Large-Span Structure with IeIs. Figure 4 illustrates a general large-span structure divided into three cases: base-fixed, LVD isolator, and IeI. H, h, L, R, and θ stand for the column height, rise, span, radius, and half-subtended angle of the roof, respectively. The LVD isolator can be ideally simulated by a parallel configuration, including a linear spring with horizontal stiffness coefficient k_{iso} and a dashpot with damping coefficient c_{iso}.

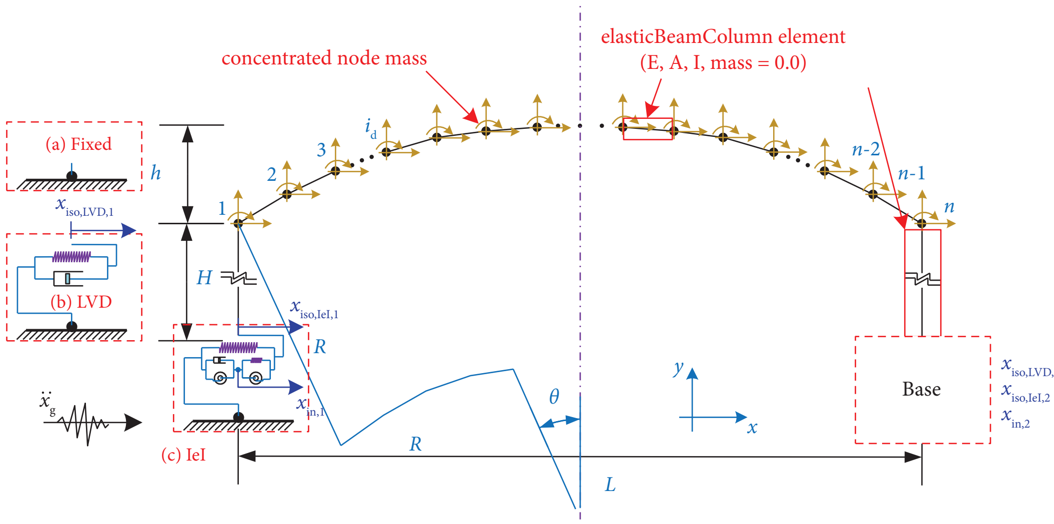

FIGURE 4: Mechanical model of the large-span structure (in OpenSees): (a) base-fixed; (b) linear viscous damper (LVD) isolator; (c) IeI.

Considering the seismic excitation case, the governing equations of the large-span structure with a fixed base can be expressed as follows:

$$\mathrm{M_p}\begin{Bmatrix}\ddot{x}_\mathrm{p}\\ \ddot{y}_\mathrm{p}\\ \ddot{\theta}_\mathrm{p}\end{Bmatrix}+\mathrm{C_p}\begin{Bmatrix}\dot{x}_\mathrm{p}\\ \dot{y}_\mathrm{p}\\ \dot{\theta}_\mathrm{p}\end{Bmatrix}+\mathrm{K_p}\begin{Bmatrix}x_\mathrm{p}\\ y_\mathrm{p}\\ \theta_\mathrm{p}\end{Bmatrix}=-\mathrm{M_p}\{\mathrm{r}\}\ddot{x}_g, \tag{3}$$

where $\{r\}$ is the influence coefficient; $\ddot{x}_g$ is the acceleration of ground motions; x_p, y_p, and θ_p are the horizontal, vertical, and rotational displacement vectors of the concentrated nodes, respectively; and $\mathrm{M_p}$, $\mathrm{C_p}$, and $\mathrm{K_p}$ are the mass matrix, damping coefficient matrix, and stiffness matrix of the primary large-span structure, respectively:

$$\begin{aligned}\mathrm{M_p}&=\begin{bmatrix}\mathrm{M_{p,x}}&0&0\\0&\mathrm{M_{p,y}}&0\\0&0&\mathrm{M_{p,\theta}}\end{bmatrix},\\ \mathrm{K_p}&=\begin{bmatrix}\mathrm{K_{p,xx}}&\mathrm{K_{p,xy}}&\mathrm{K_{p,x\theta}}\\ \mathrm{K^T_{p,xy}}&\mathrm{K_{p,yy}}&\mathrm{K_{p,y\theta}}\\ \mathrm{K^T_{p,x\theta}}&\mathrm{K^T_{p,y\theta}}&\mathrm{K_{p,\theta\theta}}\end{bmatrix},\\ \mathrm{C_p}&=\alpha_\mathrm{p}\mathrm{K_p},\end{aligned} \tag{4}$$

where $\mathrm{M_{p,x}}$, $\mathrm{M_{p,y}}$, and $\mathrm{M_{p,\theta}}$ are the mass matrices corresponding to the horizontal, vertical, and rotational degrees of freedom, respectively; and $\mathrm{K_{p,xx}}$, $\mathrm{K_{p,yy}}$, $\mathrm{K_{p,\theta\theta}}$, $\mathrm{K_{p,xy}}$, $\mathrm{K_{p,x\theta}}$, and $\mathrm{K_{p,y\theta}}$ denote the stiffness matrices representing the interrelationships among the horizontal, vertical, and rotational degrees of freedom. In this study, only stiffness-proportional damping is considered, as incorporating mass-proportional damping may result in underestimating the seismic responses of base-isolated structures [59].

By incorporating equation (2) with equation (3) and considering the mass of the isolator as $\mathrm{m_{iso}}$, the governing equations for the large-span structure with IeIs can be updated as follows:

$$\begin{bmatrix}\mathrm{M_p}&0\\0&\mathrm{M_{iso}}\end{bmatrix}\begin{Bmatrix}\ddot{x}_\mathrm{p}\\ \ddot{y}_\mathrm{p}\\ \ddot{\theta}_\mathrm{p}\\ \ddot{x}_\mathrm{iso}\end{Bmatrix}+\begin{bmatrix}\mathrm{C_p}&-\mathrm{C^T_{p,iso}}\\-\mathrm{C_{p,iso}}&\mathrm{C_{iso}}\end{bmatrix}\begin{Bmatrix}\dot{x}_\mathrm{p}\\ \dot{y}_\mathrm{p}\\ \dot{\theta}_\mathrm{p}\\ \dot{x}_\mathrm{iso}\end{Bmatrix}+\begin{bmatrix}\mathrm{K_p}&-\mathrm{K^T_{p,iso}}\\-\mathrm{K_{p,iso}}&\mathrm{K_{iso}}\end{bmatrix}\begin{Bmatrix}x_\mathrm{p}\\ y_\mathrm{p}\\ \theta_\mathrm{p}\\ x_\mathrm{iso}\end{Bmatrix}=-\begin{bmatrix}\mathrm{M_p}&0\\0&\mathrm{M'_{iso}}\end{bmatrix}\begin{Bmatrix}\mathrm{r}\\ \mathrm{r_{iso}}\end{Bmatrix}\ddot{x}_\mathrm{g}, \tag{5}$$

where

$$\mathrm{M}_{\mathrm{iso}}=\begin{bmatrix} m_{\mathrm{iso}}+m_{\mathrm{d},1} & 0 & -m_{\mathrm{d},1} & 0 \\ 0 & m_{\mathrm{iso}}+m_{\mathrm{d},1} & 0 & -m_{\mathrm{d},1} \\ -m_{\mathrm{d},1} & 0 & m_{\mathrm{d},1}+m_{\mathrm{d},2} & 0 \\ 0 & -m_{\mathrm{d},1} & 0 & m_{\mathrm{d},1}+m_{\mathrm{d},2} \end{bmatrix},$$

$$\mathrm{M}_{\mathrm{iso}}'=\begin{bmatrix} m_{\mathrm{iso}} & 0 & 0 & 0 \\ 0 & m_{\mathrm{iso}} & 0 & 0 \\ 0 & 0 & 0 & 0 \\ 0 & 0 & 0 & 0 \end{bmatrix},$$

$$\mathrm{C}_{\mathrm{iso}}=\begin{bmatrix} \alpha_{\mathrm{p}}k_{\mathrm{x}}^{\mathrm{column}} & 0 & 0 & 0 \\ 0 & \alpha_{\mathrm{p}}k_{\mathrm{x}}^{\mathrm{column}} & 0 & 0 \\ 0 & 0 & c_{\mathrm{iso}} & 0 \\ 0 & 0 & 0 & c_{\mathrm{iso}} \end{bmatrix},$$

$$\mathrm{K}_{\mathrm{iso}}=\begin{bmatrix} k_{\mathrm{iso}}+k_{\mathrm{t}}+k_{\mathrm{x}}^{\mathrm{column}} & 0 & -k_{\mathrm{t}} & 0 \\ 0 & k_{\mathrm{iso}}+k_{\mathrm{t}}+k_{\mathrm{x}}^{\mathrm{column}} & 0 & -k_{\mathrm{t}} \\ -k_{\mathrm{t}} & 0 & k_{\mathrm{t}} & 0 \\ 0 & -k_{\mathrm{t}} & 0 & k_{\mathrm{t}} \end{bmatrix}, \tag{6}$$

$$\mathrm{K}_{\mathrm{p,iso}}=\begin{bmatrix} k_{\mathrm{x}}^{\mathrm{column}} & 0_{2n_{\mathrm{p}}-1} & k_{\theta}^{\mathrm{column}} & 0_{n_{\mathrm{p}}-1} \\ 0_{n_{\mathrm{p}}-1} & k_{\mathrm{x}}^{\mathrm{column}} & 0_{2n_{\mathrm{p}}-1} & k_{\theta}^{\mathrm{column}} \\ \multicolumn{4}{c}{0_{2\times 3n_{\mathrm{p}}}} \end{bmatrix},$$

$$\mathrm{C}_{\mathrm{p,iso}}=\alpha_{\mathrm{p}}\mathrm{K}_{\mathrm{p,iso}},\mathrm{x}_{\mathrm{iso}}=\begin{Bmatrix} x_{\mathrm{iso,IeI},1} \\ x_{\mathrm{iso,IeI},2} \\ x_{\mathrm{in},1} \\ x_{\mathrm{in},2} \end{Bmatrix}.$$

The $k_{\mathrm{x}}^{\mathrm{column}}$ and $k_{\theta}^{\mathrm{column}}$ signify the horizontal and rotational stiffnesses of the column, respectively. The elements of $\mathrm{r}_{\mathrm{iso}}$ correspond to the mass of the isolator, with a value of 1, while the remaining elements are set as 0. n_{p} denotes the number of concentrated nodes employed for modeling the large-span structure. As depicted in Figure 4, $x_{\mathrm{iso,IeI},1}$ and $x_{\mathrm{iso,IeI},2}$ represent the displacements of the two used IeIs. However, $x_{\mathrm{in},1}$ and $x_{\mathrm{in},2}$ denote the displacements of the damper within the IeIs. $\mathrm{r}_{\mathrm{iso}}$ is a vector that represents the influence coefficient of IeIs.

Neglecting the torsional mass with a relatively small impact on seismic response is standard practice to minimize the degrees of freedom used in calculations. Equation (5) can be further simplified through static condensation [60], as shown as follows:

$$\mathrm{M}_{\mathrm{c,IeI}}\ddot{\mathrm{X}}_{\mathrm{c,IeI}}+\mathrm{C}_{\mathrm{c,IeI}}\dot{\mathrm{X}}_{\mathrm{c,IeI}}+\mathrm{K}_{\mathrm{c,IeI}}\mathrm{X}_{\mathrm{c,IeI}}=-\mathrm{M}_{\mathrm{c,IeI}}'\mathrm{r}_{\mathrm{c,IeI}}\ddot{x}_{\mathrm{g}}, \tag{7}$$

where

$$\mathrm{M}_{\mathrm{c,IeI}}=\begin{bmatrix} \mathrm{M}_{\mathrm{p,x}} & 0 & 0 \\ 0 & \mathrm{M}_{\mathrm{p,y}} & 0 \\ 0 & 0 & \mathrm{M}_{\mathrm{iso}} \end{bmatrix},$$

$$\mathrm{M}_{\mathrm{c,IeI}}'=\begin{bmatrix} \mathrm{M}_{\mathrm{p,x}} & 0 & 0 \\ 0 & \mathrm{M}_{\mathrm{p,y}} & 0 \\ 0 & 0 & \mathrm{M}_{\mathrm{iso}}' \end{bmatrix},$$

$$\mathrm{X}_{\mathrm{c,IeI}}=\begin{Bmatrix} \mathrm{x}_{\mathrm{p}} \\ \mathrm{y}_{\mathrm{p}} \\ \mathrm{x}_{\mathrm{iso}} \end{Bmatrix}, \tag{8}$$

$$\mathrm{K}_{\mathrm{c,IeI}}=\mathrm{K}_{\mathrm{T}}-\mathrm{K}_{\mathrm{T}\theta}\mathrm{K}_{\theta}^{-1}\mathrm{K}_{\mathrm{T}\theta}^{T},$$

$$\mathrm{C}_{\mathrm{c,IeI}}=\mathrm{C}_{\mathrm{T}}-\mathrm{C}_{\mathrm{T}\theta}\mathrm{C}_{\theta}^{-1}\mathrm{C}_{\mathrm{T}\theta}^{T}.$$

$\mathrm{K_T}$, $\mathrm{K_{T\theta}}$, and $\mathrm{K_\theta}$ are obtained by reorganizing the stiffness matrix in equation (5) based on translational displacements and rotations. $\mathrm{C_T}$, $\mathrm{C_{T\theta}}$, and $\mathrm{C_\theta}$ are obtained by reorganizing the damping matrix in equation (5) based on translational displacements and rotations. $\mathrm{r_{c,IeI}}$ represents the influence vector obtained by removing the elements corresponding to rotational degrees of freedom.

3. Input Energy Reduction-Oriented Design of the IeI-Equipped Large-Span Structures

Building on the governing equations formulated in the previous section, this section elucidates the principle of input energy reduction for structures controlled by grounded inerters within the IeI. A stochastic energy analysis method is employed to quantify and compare the energy performance of large-span structures equipped with either IeIs or conventional LVD isolators. Through a comprehensive parametric investigation, the superior effectiveness of the IeI over the LVD isolator is demonstrated. This analysis leads to the development of a design approach that is specifically oriented towards maximizing input energy reduction in the IeI.

3.1. Overview of Input Energy Reduction. According to equation (7), the governing equations of the large-span structure with IeIs have different mass matrices on the left and right sides, where the apparent mass and physical mass dominate, respectively [51]. Owing to the negligible physical mass of the inerter, its grounded installation increases the structural inertia through its apparent mass without impacting the seismic input force. Generally, the grounded inerter within the IeI can equivalently reduce the amplitude of input seismic acceleration, resulting in a decreased energy power of the ground motion input into the structure. Taking white noise as an example of input, the input energy power can be depicted by the slope of lines in Figure 5. Consequently, the height of the plateau segment, illustrating the total input energy, can be reduced by introducing and optimizing the series grounded inerters into the IeI for large-span structures. A more detailed analysis will be provided in subsequent discussions, focusing on defining energy indexes and conducting a detailed parametric analysis to further elucidate these findings.

3.2. Stochastic Energy Analysis. A comprehensive understanding of the isolation mechanism of the IeI can be achieved by investigating the transfer pathways and distribution of seismic energy between the isolators and the superstructures. Considering the inherent stochastic feature of seismic ground motions, the statistical values derived from the stochastic response analysis are adopted as quantitative indicators.

Assuming the ground motion acceleration as a Gaussian white noise $w(t)$, the reduced motion equation for the large-span structure with IeIs in equation (7) can be rewritten as a state-space-variable compact form:

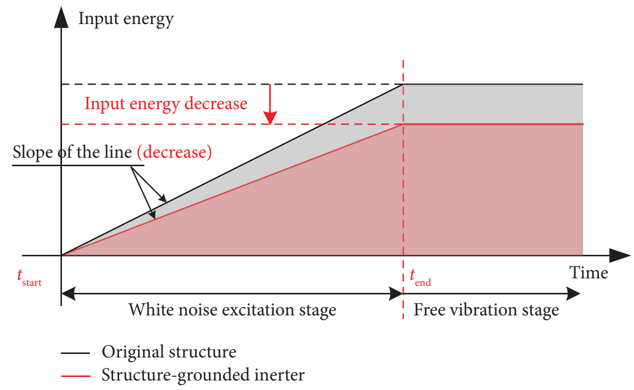

Figure 5: Schematic representation of the input energy reduction.

$$\dot{\mathrm{X}}_{\mathrm{s,IeI}}(t) = \mathrm{A_{s,IeI}}\mathrm{X_{s,IeI}}(t) + \mathrm{E_{s,IeI}}w(t), \tag{9}$$

where

$$\mathrm{X_{s,IeI}}(t) = \begin{bmatrix} \mathrm{X_{c,IeI}} \\ \dot{\mathrm{X}}_{\mathrm{c,IeI}} \end{bmatrix},$$
$$\mathrm{A_{s,IeI}} = \begin{bmatrix} 0 & \mathrm{I} \\ -\mathrm{M_{c,IeI}}^{-1}\mathrm{K_{c,IeI}} & -\mathrm{M_{c,IeI}}^{-1}\mathrm{C_{c,IeI}} \end{bmatrix}, \tag{10}$$
$$\mathrm{E_{s,IeI}} = \begin{bmatrix} 0 \\ \mathrm{M_{c,IeI}}^{-1}\mathrm{M}'_{\mathrm{c,IeI}}\mathrm{r_{c,IeI}} \end{bmatrix}.$$

The direct stochastic analysis method [61] ensures that the state variable covariance matrices can be obtained by solving the following Lyapunov equation:

$$\mathrm{A_{s,IeI}}\mathrm{P_{s,IeI}} + \mathrm{P}^T_{\mathrm{s,IeI}}\mathrm{A_{s,IeI}} + \mathrm{E_{s,IeI}}\mathrm{E}^T_{\mathrm{s,IeI}} = 0, \tag{11}$$

where $\mathrm{P_{s,IeI}}$ is the covariance matrix of the state variables of the large-span structure with IeIs.

By multiplying equation (7) on the left with $\dot{\mathrm{X}}^T_{\mathrm{s,IeI}}$ and integrating each term over the entire time domain, the following energy balance equation of the large-span structure with IeIs can be obtained:

$$E_{\mathrm{k,IeI}} + E_{\mathrm{d,IeI}} + E_{\mathrm{e,IeI}} = E_{\mathrm{in,IeI}}, \tag{12}$$

where

$$\begin{cases} E_{\mathrm{k,IeI}} = \int_0^\infty \dot{\mathrm{X}}^T_{\mathrm{s,IeI}}\mathrm{M_{c,IeI}}\ddot{\mathrm{X}}_{\mathrm{c,IeI}}dt, \\ E_{\mathrm{d,IeI}} = \int_0^\infty \dot{\mathrm{X}}^T_{\mathrm{s,IeI}}\mathrm{C_{c,IeI}}\dot{\mathrm{X}}_{\mathrm{c,IeI}}dt, \\ E_{\mathrm{e,IeI}} = \int_0^\infty \dot{\mathrm{X}}^T_{\mathrm{s,IeI}}\mathrm{K_{c,IeI}}\mathrm{X_{c,IeI}}dt, \\ E_{\mathrm{in,IeI}} = \int_0^\infty \dot{\mathrm{X}}^T_{\mathrm{s,IeI}}\mathrm{M}'_{\mathrm{c,IeI}}\mathrm{r_{c,IeI}}\ddot{x}_g dt. \end{cases} \tag{13}$$

$E_{\mathrm{k,IeI}}$, $E_{\mathrm{d,IeI}}$, $E_{\mathrm{e,IeI}}$, and $E_{\mathrm{in,IeI}}$, respectively, represent the kinetic energy, damping dissipated energy, elastic strain energy, and the overall input energy of the large-span structure with IeIs. Traditionally, both the initial and final states are assumed to be stationary:

$$\begin{cases} \mathrm{X}_{\mathrm{c,IeI}}(0) = 0, \dot{\mathrm{X}}_{\mathrm{c,IeI}}(0) = 0, \ddot{\mathrm{X}}_{\mathrm{c,IeI}}(0) = 0, \\ \mathrm{X}_{\mathrm{c,IeI}}(\infty) = 0, \dot{\mathrm{X}}_{\mathrm{c,IeI}}(\infty) = 0, \ddot{\mathrm{X}}_{\mathrm{c,IeI}}(\infty) = 0. \end{cases} \tag{14}$$

Substituting equation (14) into equation (13), the matrix operations can be expanded and correspondingly yield

$$\begin{cases} E_{\mathrm{k,IeI}} = \sum_{i=1}^{n_{\mathrm{p}}+4} \sum_{j=1}^{n_{\mathrm{p}}+4} \left[M_{\mathrm{c,IeI}}^{(i,j)} \cdot \int_0^\infty \dot{X}_{\mathrm{c,IeI}}^{(i)} \ddot{X}_{\mathrm{c,IeI}}^{(j)} dt \right] = 0, \\ E_{\mathrm{d,IeI}} = \sum_{i=1}^{n_{\mathrm{p}}+4} \sum_{j=1}^{n_{\mathrm{p}}+4} \left[C_{\mathrm{c,IeI}}^{(i,j)} \cdot \int_0^\infty \dot{X}_{\mathrm{c,IeI}}^{(i)} \dot{X}_{\mathrm{c,IeI}}^{(j)} dt \right] = \sum_{i=1}^{n_{\mathrm{p}}+4} \sum_{j=1}^{n_{\mathrm{p}}+4} \left[C_{\mathrm{c,p}}^{(i,j)} \cdot COV\left(\dot{X}_{\mathrm{c,p}}^{(i)}, \dot{X}_{\mathrm{c,p}}^{(j)} \right) \right], \\ E_{\mathrm{e,IeI}} = \sum_{i=1}^{n_{\mathrm{p}}+4} \sum_{j=1}^{n_{\mathrm{p}}+4} \left[K_{\mathrm{c,IeI}}^{(i,j)} \cdot \int_0^\infty \dot{X}_{\mathrm{c,IeI}}^{(i)} X_{\mathrm{c,IeI}}^{(j)} dt \right] = 0, \end{cases} \tag{15}$$

where n_{p} refers to the number of concentrated nodes employed for modeling the large-span structure; $M_{\mathrm{c,IeI}}^{(i,j)}$, $C_{\mathrm{c,IeI}}^{(i,j)}$, and $K_{\mathrm{c,IeI}}^{(i,j)}$, respectively, represent the i^{th} row and j^{th} column elements of matrices $\mathrm{M}_{\mathrm{c,IeI}}$, $\mathrm{C}_{\mathrm{c,IeI}}$, and $\mathrm{K}_{\mathrm{c,IeI}}$; $X_{\mathrm{c,IeI}}^{(i)}$ and $X_{\mathrm{c,IeI}}^{(j)}$, respectively, denote the i^{th} row and j^{th} row elements of the vector $\mathrm{X}_{\mathrm{c,IeI}}$; and $COV(-)$ denotes the cross-covariance operator; referring to [62], the expression for $E_{\mathrm{d,IeI}}$ in formula (15) can be compactly represented in matrix form as follows:

$$E_{\mathrm{d,IeI}} = \tau_{\mathrm{IeI}}^T \left(\mathrm{C}_{\mathrm{c,IeI}} .* \sum_{\dot{X}_{\mathrm{c,IeI}} \dot{X}_{\mathrm{c,IeI}}} \right) \tau_{\mathrm{IeI}}, \tag{16}$$

where τ_{IeI} is an $n_p + 4$ column unit vector; $\Sigma_{\dot{X}_{\mathrm{c,IeI}} \dot{X}_{\mathrm{c,IeI}}}$ denotes the covariance matrix of the velocity responses of the large-span structure with IeIs, which can be obtained from the state covariance matrix $P_{\mathrm{s,IeI}}$; and the symbol *denotes the MATLAB element-wise multiplication operator; the energy balance principle ensures that the overall input energy of the large-span structure with IeIs $E_{\mathrm{in,IeI}}$ can be expressed as

$$E_{\mathrm{in,IeI}} = E_{\mathrm{d,IeI}} = \tau_{\mathrm{IeI}}{}^T \left(\mathrm{C}_{\mathrm{c,IeI}} .* \sum_{\dot{X}_{\mathrm{c,IeI}} \dot{X}_{\mathrm{c,IeI}}} \right) \tau_{\mathrm{IeI}}. \tag{17}$$

Furthermore, the energy dissipated by the dashpots in IeIs, namely, $E_{\mathrm{damper,IeI}}$, can be expressed as follows:

$$\begin{aligned} E_{\mathrm{damper,IeI}} &= \int_0^\infty \dot{x}_{\mathrm{in,1}}^{\mathrm{T}} c_{\mathrm{iso}} \dot{x}_{\mathrm{in,1}}^{\mathrm{T}} dt + \int_0^\infty \dot{x}_{\mathrm{in,2}}^{\mathrm{T}} c_{\mathrm{iso}} \dot{x}_{\mathrm{in,2}}^{\mathrm{T}} dt \\ &= c_{\mathrm{iso}} \left(\sigma_{\dot{x}_{\mathrm{in,1}}}^2 + \sigma_{\dot{x}_{\mathrm{in,2}}}^2 \right), \end{aligned} \tag{18}$$

where $\sigma_{\dot{x}_{\mathrm{in,1}}}$ and $\sigma_{\dot{x}_{\mathrm{in,1}}}$ denote the root-mean-square velocity responses of the two IeI isolation layers and can be obtained as the corresponding diagonal elements of the state covariance matrix $P_{\mathrm{s,IeI}}$.

Hence, the energy balance principle ensures that the dissipated energy of the superstructure within large-span structure with IeIs, $E_{\mathrm{ds,IeI}}$, can be finally described as

$$E_{\mathrm{ds,IeI}} = E_{\mathrm{d,IeI}} - E_{\mathrm{damper,IeI}}. \tag{19}$$

In the same manner, the overall input energy and the energy dissipated by the dashpot and superstructure of the large-span structures with LVD isolators, namely, $E_{\mathrm{in,LVD}}$, $E_{\mathrm{damper,LVD}}$, and $E_{\mathrm{ds,LVD}}$, can be derived. Detailed information can be found in Appendix B.

3.3. Parametric Investigation and Discussion. From the perspective of energy performances and control performances, the functionality of IeI key parameters, including $m_{\mathrm{d,1}}$, $m_{\mathrm{d,2}}$, k_{iso}, k_{t}, and c_{iso}, is investigated on the following aspects: (1) the overall input energy of the whole large-span structure with IeIs; (2) the dissipated energy of the superstructure; (3) the displacement response of the isolator; and (4) the damping enhancement effect. To facilitate the representation and consider the structural symmetry, the following dimensionless parameters are defined and employed in the parametric analysis:

$$\mu_{\mathrm{d}} = \frac{m_{\mathrm{d},1} + m_{\mathrm{d},2}}{M_0},$$
$$\kappa_{\mathrm{t}} = \frac{k_{\mathrm{in}}}{k_{\mathrm{iso}}},$$
$$\xi_{\mathrm{iso}} = \frac{c_{\mathrm{iso}}}{2M_0\omega_0}, \tag{20}$$
$$\gamma_\mu = \frac{m_{\mathrm{d},1}}{m_{\mathrm{d},1} + m_{\mathrm{d},2}},$$

where M_0 represents the total mass of the half-structure and ω_0 denotes the natural frequency of the large-span structure. μ_{d}, κ_{t}, and ξ_{iso} refer to the inertance-mass ratio, stiffness ratio, and damping ratio of the IeI. The inertance-distribution ratio, which indicates the apparent mass distribution between two inerters in the IeI, is denoted by γ_μ.

3.3.1. Energy Index. Based on stochastic energy analysis, the normalized overall input energy, denoted as $\overline{E_{\mathrm{in,LVD}}}$ or $\overline{E_{\mathrm{in,IeI}}}$, can be defined for the large-span structure equipped with IeIs or the LVD isolators. The normalization is based on half the mass of the overall structure of the large-span structure, including the isolation layer:

$$\overline{E_{\mathrm{in,LVD}}} = \frac{E_{\mathrm{in,LVD}}}{M_0 + m_{\mathrm{iso}}}, \overline{E_{\mathrm{in,IeI}}} = \frac{E_{\mathrm{in,IeI}}}{M_0 + m_{\mathrm{iso}}}. \tag{21}$$

As shown in Figure 6, for the large-span structure with LVD isolators, the input energy remains constant regardless of the damping ratio ξ_{iso}. The value of $\overline{E_{\mathrm{in,LVD}}}$ close to 1 implies that the conclusion previously established for typical shear structures [63] is applicable to large-span structures with LVD isolators as well. In particular, this conclusion states that the value of the overall input energy of a structure under unit white noise excitation numerically approximates half the total structural mass. Both Figures 6(a) and 6(b) demonstrate that the stiffness ratio κ_t and damping ratio ξ_{iso} have no discernible impact on the overall input energy, while the increase in the inertance-mass ratio μ_d leads to a significant decrease in the input energy. Figure 6(c) illustrates the input energy of the large-span structure with IeIs influenced by the inertance-distribution ratio γ_μ. As the inertance-distribution ratio γ_μ increases, the input energy initially decreases and then increases, reaching its minimum at $\gamma_\mu = 0.5$. Therefore, to maximize the use of the IeI for a high-efficiency input energy reduction, the γ_μ is theoretically optimized as 0.5 in the subsequent analysis.

Additionally, from the configuration of dashpot, inerters, and tuning spring in Figure 1, it can be observed that for $\gamma_\mu = 0.0$, the IeI configuration aligns with TVMD-based isolation system, whereas for $\gamma_\mu = 1.0$, the IeI configuration aligns with a tuned inerter braced damper (TIBD)-based isolation system. In the condition of inertance-mass ratio $\mu_d = 0.0$ and stiffness ratio κ_t approaching infinity, the IeI degenerates into a LVD isolator. Consistent with previous research findings [51], TVMD-, TIBD-, and LVD-based isolation devices are useless for the desired input energy reduction, verifying the unique effectiveness and design of the IeI for the released energy dissipation burden of this complex large-span structure.

Following the same normalization process, the normalized energy dissipated by the superstructure, denoted as $\overline{E_{\mathrm{ds,LVD}}}$ or $\overline{E_{\mathrm{ds,IeI}}}$, can be defined for the large-span structure equipped with IeIs or the LVD isolators:

$$\overline{E_{\mathrm{ds,LVD}}} = \frac{E_{\mathrm{ds,LVD}}}{M_0 + m_{\mathrm{iso}}}, \overline{E_{\mathrm{ds,IeI}}} = \frac{E_{\mathrm{ds,IeI}}}{M_0 + m_{\mathrm{iso}}}. \tag{22}$$

As presented in Figure 7(a) for the large-span structure with conventional LVD isolators, when the stiffness ratio κ_{iso} of the isolator decreases and the damping ratio ξ_{iso} increases, indicative of an isolator with softer resistance and higher damping capacity, the energy dissipated by the superstructure is notably reduced. Figures 7(b), 7(c), and 7(d) depict the normalized energy dissipated by the superstructure for the IeI case. In this scenario, the stiffness ratio κ_{iso} and damping ratio ξ_{iso} are predetermined from the LVD isolator case, aiming to dissipate 50%, 30%, and 10% of the isolator based on the LVD isolator configuration, with the objective of dissipating 50%, 30%, and 10% of the seismic input energy by the superstructure while considering a specific constraint on the displacement of the isolator. Detailed design methodologies will be elaborated in Section 3.3. The results identify an optimal combination of the stiffness ratio κ_{t} and the inertance-mass ratio μ_d at the minimum of the contour plot, demonstrating the IeI's effectiveness in reducing the energy dissipated by the superstructure compared with the traditional LVD isolator condition. Furthermore, it is apparent that when the stiffness ratio κ_t and the mass ratio μ_d are not properly aligned, especially when the stiffness ratio κ_t is too low, the performance of the IeI is inferior to that of the LVD isolator. This disparity arises because the mismatch between the stiffness ratio κ_t and the mass ratio μ_d hinders the effective transmission of displacement from the isolation layer to the dashpot within the IeI, thereby diminishing its energy absorption capacity. Therefore, it is crucial to ensure the proper alignment of the stiffness ratio κ_t and mass ratio μ_d when designing the IeI. Comparison of Figures 7(b), 7(c), and 7(d) reveals that as the requirements for isolating performance intensify, resulting in greater reductions in energy dissipation by the superstructure, the marginal performance gains provided by IeI over the conventional LVD isolator diminish. Even considering an LVD isolator that isolates 90% of the seismic input energy, as illustrated in Figure 7(d), the IeI still achieves a performance enhancement of approximately 24%, unattainable with the standard LVD isolation system. This achievement indicates a substantial decrease in displacement relative to the isolator, acceleration, and base shear forces affecting the large-span structure, which will be further discussed in the subsequent section.

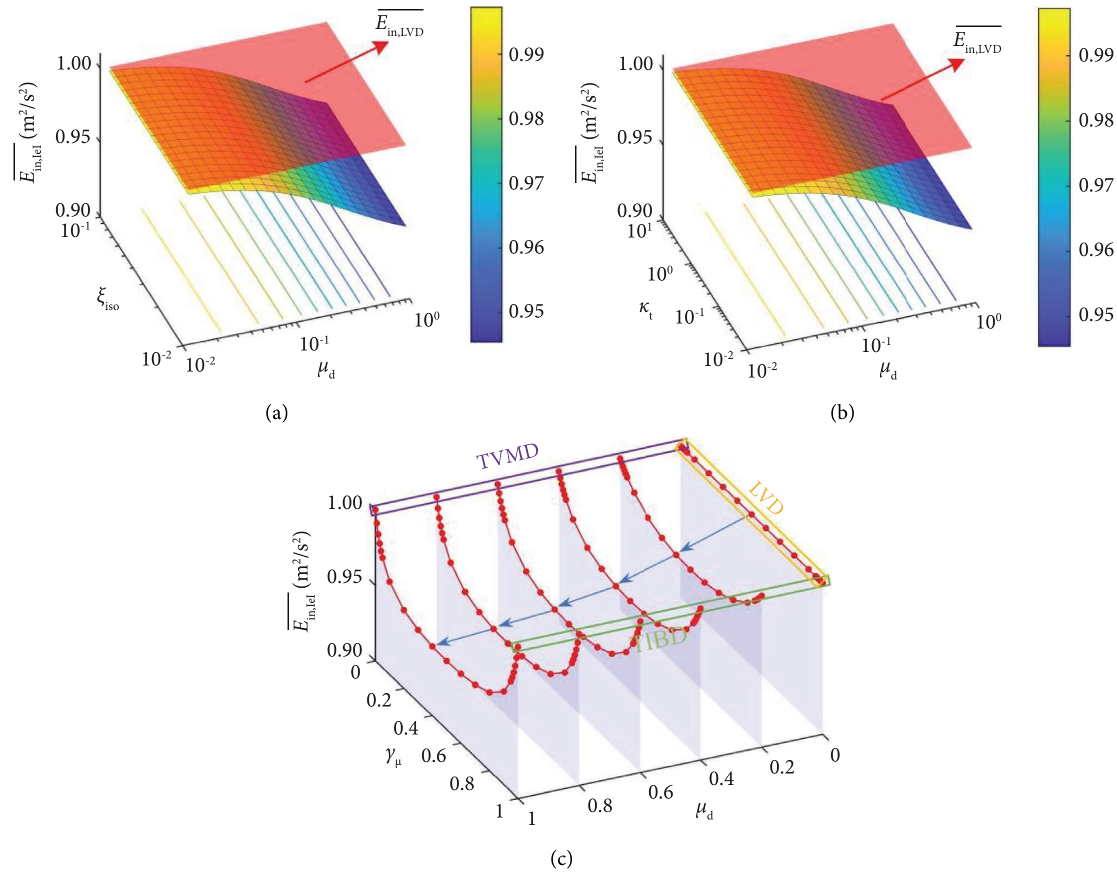

FIGURE 6: Input energy of the large-span structures with IeIs or LVD isolators. (a) $\mu_d \in [10^{-2}, 1]$ and $\xi_{iso} \in [10^{-2}, 10^{-1}]$; (b) $\mu_d \in [10^{-2}, 1]$ and $k_t \in [10^{-2}, 10]$; (c) $\mu_d \in [0, 1]$ and $\gamma_\mu \in [0, 1]$.

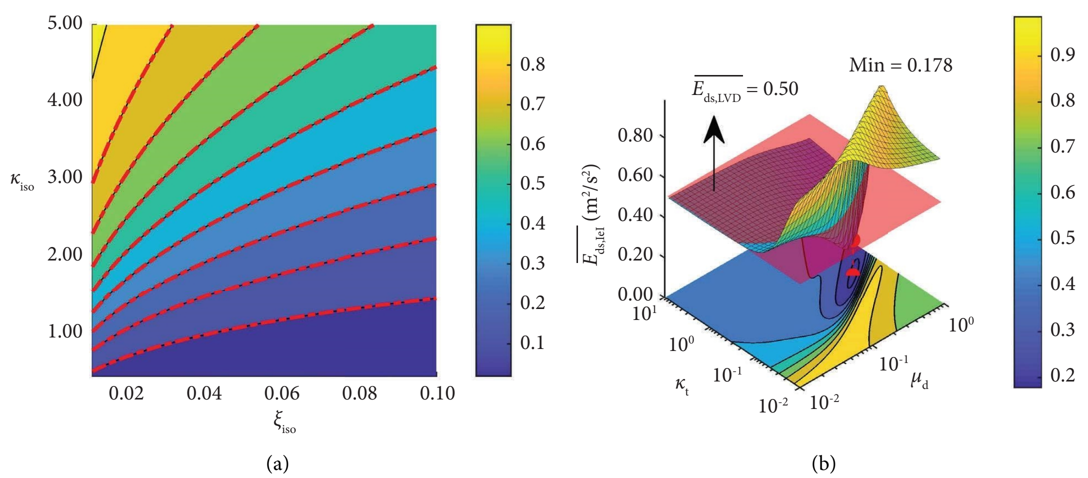

FIGURE 7: Continued.

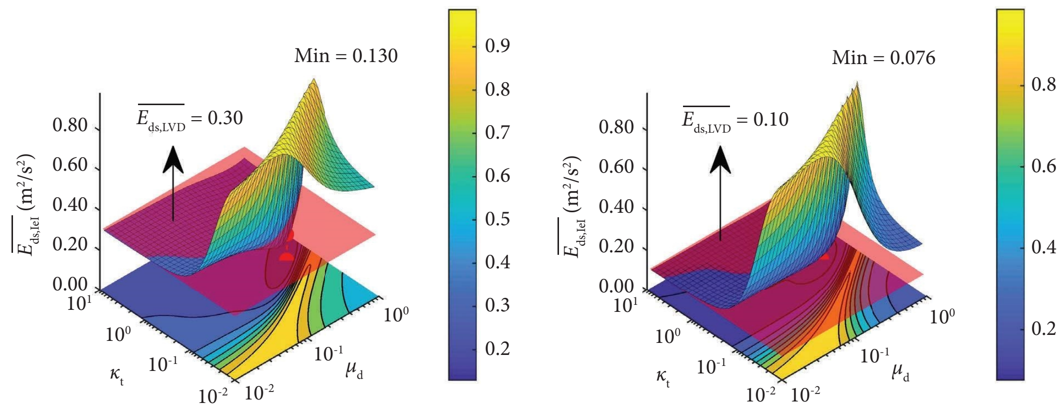

Figure 7: Normalized superstructure dissipated energy of the large-span structures with IeIs or LVD isolators: (a) LVD isolator ($\mu_d = 0$, $\kappa_t = \infty$, $\kappa_{\mathrm{iso}} \in [10^{-2}, 5.00]$, and $\xi_{\mathrm{iso}} \in [10^{-2}, 10^{-1}]$); (b) IeI ($\mu_d \in [10^{-2}, 1]$, $\kappa_t \in [10^{-2}, 10]$, $\xi_{\mathrm{iso}} = 0.024$, and $\kappa_{\mathrm{iso}} = 2.353$); (c) IeI ($\mu_d \in [10^{-2}, 1]$, $\kappa_t \in 10^{-2}, 10]$, $\xi_{\mathrm{iso}} = 0.038$, and $\kappa_{\mathrm{iso}} = 1.937$); (d) IeI ($\mu_d \in [10^{-2}, 1]$, $\kappa_t \in [10^{-2}, 10]$, $\xi_{\mathrm{iso}} = 0.066$, and $\kappa_{\mathrm{iso}} = 1.269$).

3.3.2. Isolator Displacement Performance Index. Based on the demonstrated advantages of the IeI for energy input and dissipation, the primary concerns continue to be the mitigation levels of seismic responses and the performance of the isolation layer. All isolator displacement responses are normalized by the maximum RMS value of nodal displacement observed in the uncontrolled large-span structure. These indexes for normalized displacement-related performance are delineated as follows:

$$\overline{\sigma_{\mathrm{iso,LVD}}} = \frac{\max\left\{\sigma_{\mathrm{iso,LVD,1}}, \sigma_{\mathrm{iso,LVD,2}}\right\}}{\sigma_{0,\max}},$$
$$\overline{\sigma_{\mathrm{iso,IeI}}} = \frac{\max\left\{\sigma_{\mathrm{iso,IeI,1}}, \sigma_{\mathrm{iso,IeI,2}}\right\}}{\sigma_{0,\max}}, \tag{23}$$
$$\gamma_{\mathrm{IeI}} = \frac{\sigma_{\mathrm{in,1}}}{\sigma_{\mathrm{iso,IeI,1}}},$$

where $\sigma_{\mathrm{iso,LVD,1}}$ and $\sigma_{\mathrm{iso,LVD,2}}$ denote the RMS isolator displacement responses for two LVD isolators; $\sigma_{\mathrm{iso,IeI,1}}$ and $\sigma_{\mathrm{iso,IeI,2}}$ denote the RMS isolator displacement responses for two IeIs; $\sigma_{0,\max}$ represents the maximum RMS value of the nodal displacement observed in the uncontrolled large-span structure; and $\sigma_{\mathrm{in,1}}$ represents the RMS displacement response of dashpot in the IeI. The parameter γ_{IeI} denotes the ratio of the RMS displacement response of the dashpot to that of the isolator layer.

Figure 8 delineates the RMS values of isolator displacements, which are influenced by critical parameters, such as the stiffness ratio κ_{iso}, damping ratio ξ_{iso}, inertance-mass ratio μ_d, and stiffness ratio κ_t, in the context of employing either LVD isolators or IeIs for isolating the large-span structure. Figure 8(a) illustrates that an increase in the stiffness ratio κ_{iso} and damping ratio ξ_{iso} leads to effective suppression of isolator displacements. In Figures 8(b), 8(c), and 8(d), an optimal parameter set comprising the stiffness ratio κ_t and inertance-mass ratio μ_d can be identified at the minima within the contour plots. These adjustments facilitate a reduction in isolator displacements, even when the damping and stiffness coefficients remain constant relative to the LVD isolators. Figures 9(a), 9(b), and 9(c) present the correlation between dashpot displacement in the IeI and isolator layer displacement. The translucent red plane in these figures indicates scenarios where the dashpot displacement correlates directly with the isolator layer displacement, akin to observations in LVD isolators. Figures 9(a), 9(b), and 9(c) demonstrate that selecting optimal combinations of stiffness ratio κ_t and inertance-mass ratio μ_d can enhance the displacement of the dashpot while maintaining a constant isolator layer displacement, correspondingly leading to an enhanced damping efficiency for the reduced isolating space demand. Furthermore, the increase in isolating performance from Figures 9(a), 9(b), and 9(c) corresponds with a diminishing effectiveness in energy dissipation enhancement, denoted by a lower peak γ_{IeI}. This phenomenon elucidates the diminishing returns in enhancing energy dissipation in the superstructure as well, as evidenced in Figure 7.

3.4. Input Energy Reduction-Oriented Design Flowchart. Based on the parametric analysis results, the normalized superstructure dissipated energy and the normalized RMS isolator displacement of the LVD isolator are depicted in Figure 10(a) using dashed and solid lines, respectively. It can be inferred that when the damping ratio ξ_{iso} is held constant, changes in isolator stiffness yield opposite effects on the superstructure dissipated energy and the isolator displacement. In other words, for a given damping ratio ξ_{iso}, an optimal isolator stiffness exists that achieves a well-balanced performance in terms of the superstructure dissipated energy and the isolator displacement for a large-span structure isolated by the LVD isolator. These optimal points are represented by the solid red dots in Figure 10(a). Inspired by the distinguished variation pattern and vibration isolating benefits of the IeI, an input energy reduction-oriented

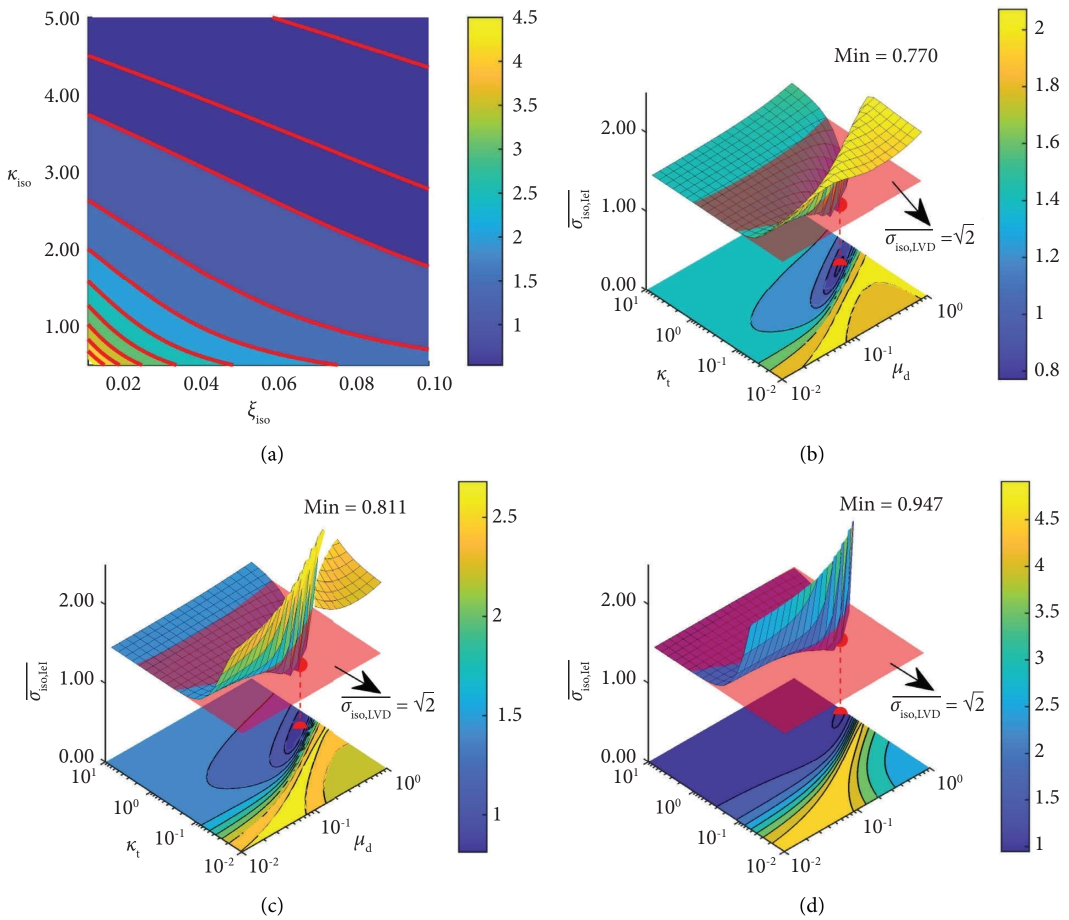

Figure 8: Normalized RMS isolator displacements of the large-span structures with IeIs or LVD isolators. (a) LVD isolator ($\mu_d = 0$, $\kappa_t = \infty$, $\kappa_{\mathrm{iso}} \in [10^{-2}, 5.00]$, and $\xi_{\mathrm{iso}} \in [10^{-2}, 10^{-1}]$); (b) IeI ($\mu_d \in [10^{-2}, 1]$, $\kappa_t \in [10^{-2}, 10]$, $\xi_{\mathrm{iso}} = 0.024$, and $\kappa_{\mathrm{iso}} = 2.353$); (c) IeI ($\mu_d \in [10^{-2}, 1]$, $\kappa_t \in [10^{-2}, 10]$, $\xi_{\mathrm{iso}} = 0.038$, and $\kappa_{\mathrm{iso}} = 1.937$); (d) IeI ($\mu_d \in [10^{-2}, 1]$, $\kappa_t \in [10^{-2}, 10]$, $\xi_{\mathrm{iso}} = 0.066$, and $\kappa_{\mathrm{iso}} = 1.269$).

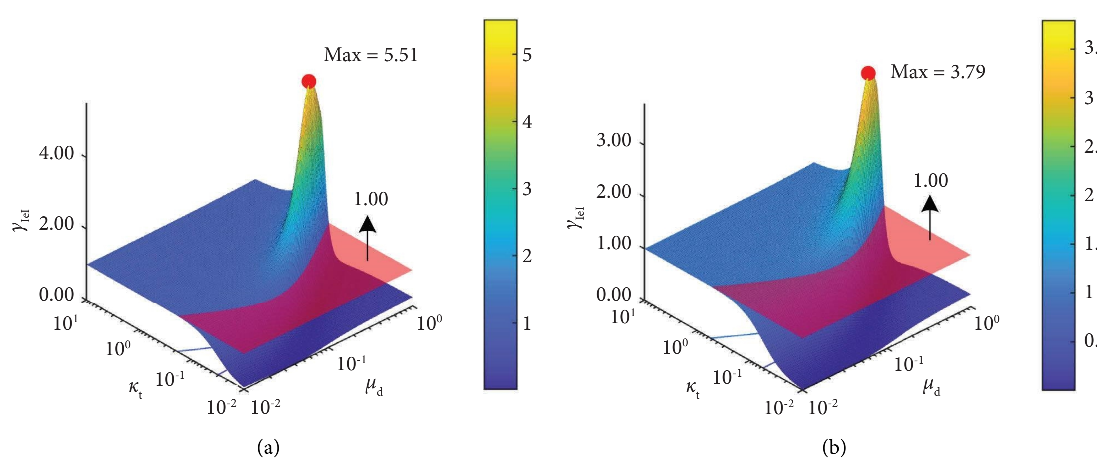

Figure 9: Continued.

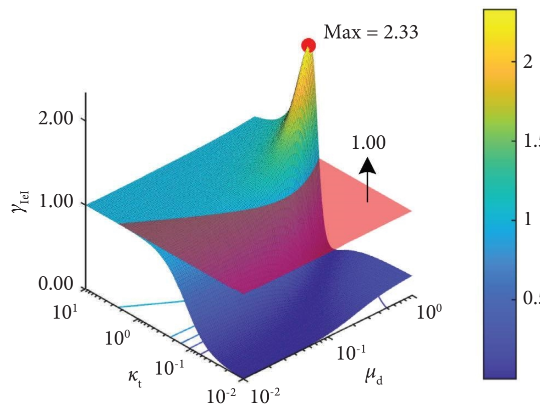

(c)

FIGURE 9: Damping enhancement index γ_{IeI} of the large-span structures with IeIs. (a) IeI ($\mu_d \in [10^{-2}, 1]$, $\kappa_t \in [10^{-2}, 10]$, $\xi_{\mathrm{iso}} = 0.024$, and $\kappa_{\mathrm{iso}} = 2.353$); (b) IeI ($\mu_d \in [10^{-2}, 1]$, $\kappa_t \in [10^{-2}, 10]$, $\xi_{\mathrm{iso}} = 0.038$, and $\kappa_{\mathrm{iso}} = 1.937$); (c) IeI ($\mu_d \in [10^{-2}, 1]$, $\kappa_t \in [10^{-2}, 10]$, the damping ratio $\xi_{\mathrm{iso}} = 0.066$, and the stiffness ratio $\kappa_{\mathrm{iso}} = 1.269$).

optimal design strategy is developed for the IeI, as illustrated in the design flowchart in Figure 11. The optimization results are shown in Figure 10(b) with the contour lines of the normalized superstructure dissipated energy and the normalized RMS isolator displacement of the IeI. Each point in Figure 10(b) represents a unique set of design parameters (κ_{iso}, ξ_{iso}, κ_{t}, μ_d), which can be directly employed in the primary design of practical applications.

The design procedure, as shown in Figure 11, can be further detailed as follows:

Step 1: Conduct preliminary analysis on the uncontrolled large-span structure to calculate the maximum RMS value of nodal displacements. Determine the performance demands based on engineering needs.

Step 2: Based on the performance demands and the preliminary analysis of the large-span structure, establish the target energy dissipation index for the superstructure and the isolator displacement index for the isolator.

Step 3: Formulate the following optimization design equations and solve them to obtain the optimal parameter set, denoted as ν^{opt}:

$$\begin{aligned} &\underset{\nu \in V}{\text{minimize}}\, \xi_{\mathrm{iso}} \\ &s.t.\ \overline{E_{\mathrm{ds,IeI}}} \le E_{\mathrm{ds,target}}, \overline{\sigma_{\mathrm{iso}}} \le \sigma_{\mathrm{iso,target}}, \end{aligned} \tag{24}$$

where $\nu = \{\kappa_{\mathrm{iso}}, \xi_{\mathrm{iso}}, \kappa_{\mathrm{t}}, \mu_{\mathrm{d}}\}$ is the set of parameters and V is the feasibility domain. V is calculated as follows:

$$V = \begin{cases} \kappa_{\mathrm{iso,\,min}} \le \kappa_{\mathrm{iso}} \le \kappa_{\mathrm{iso,\,max}}, \\ \xi_{\mathrm{iso,\,min}} \le \xi_{\mathrm{iso}} \le \xi_{\mathrm{iso,\,max}}, \\ \kappa_{\mathrm{t,\,min}} \le \kappa_{\mathrm{t}} \le \kappa_{\mathrm{t,\,max}}, \\ \mu_{\mathrm{d,\,min}} \le \mu_{\mathrm{d}} \le \mu_{\mathrm{d,\,max}}. \end{cases} \tag{25}$$

The minimization of damping ratio ξ_{iso} can be reached by pursuing the high-level input energy reduction and damping enhancement effects.

Step 4: Verify whether the performance of the designed IeI meets the engineering requirements. If it does, conclude the design process. Return to Step 1 and redefine the relevant indexes if it does not.

4. Case Design and Illustration

In this section, we use a benchmark large-span structure [19] to illustrate the design procedure of the IeI and validate its superior performance compared with the LVD isolator. As shown in Figure 12, the structure has a column height of 15.0 m, a rise of 5.2 m, a span of 79.0 m, a roof radius of 152.6 m, and a half-subtended angle of 15.0°. All materials have Young's modulus of $2.05 \times 10^5\,\mathrm{N/mm^2}$. The cross-sectional area of arch beams is $5.38 \times 10^4\,\mathrm{mm^2}$, and the cross-sectional area of the columns is $5.89 \times 10^4\,\mathrm{mm^2}$. The second moments of the arch beam and column section are $1.18 \times 10^{10}\,\mathrm{mm^4}$ and $1.35 \times 10^{10}\,\mathrm{mm^4}$, respectively. The structure has 13 discrete nodes ($n = 13$). Each node on the arch beam represents a concentrated mass of 6000 kg, equivalent to 976 kg of mass per unit length of the arch beam. In addition, the mass of each isolator is set at 3000 kg. Only stiffness-proportional damping with a first modal damping ratio of 2% for the uncontrolled structure is considered, as mass-proportional damping can lead to underestimating the seismic responses [61].

The design procedure of the IeI for the seismic response mitigation of the benchmark large-span structure is outlined as follows, following the design flowchart presented in Figure 11.

Step 1: Preanalysis of the uncontrolled original large-span structure

Based on the specimens of the structure, it can be determined that the total mass of the half-roof, M_0, is 39,000 kg, the natural frequency of the large-span structure, ω_0, is 6.76 rad/s, and the second-order frequency is 7.94 rad/s. Assuming the ground motion is Gaussian white noise, solving the Lyapunov equation in

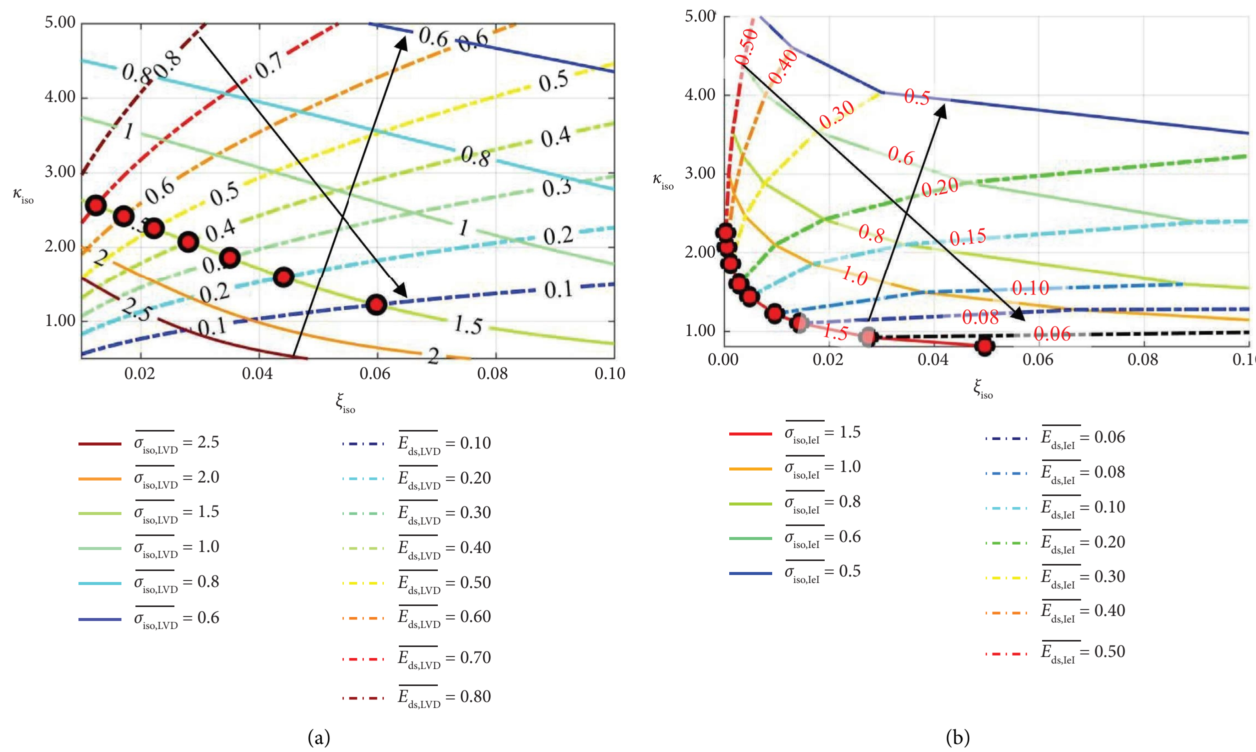

FIGURE 10: The intersection points of the contour lines. (a) LVD isolator ($\mu_d = 0$ and $\kappa_t = \infty$); (b) IeI (κ_t and μ_d are optimized by the input energy reduction-oriented design flowchart).

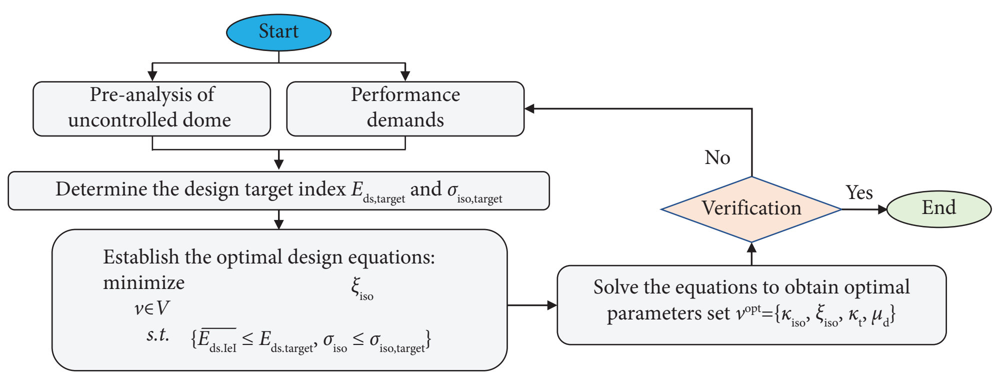

FIGURE 11: Input energy reduction-oriented design flowchart for the IeI.

equation (11) reveals that the maximum horizontal RMS displacement response is 0.111 m.

Step 2: Determination of the design target index

Specific design target indexes are determined based on practical requirements, such as deformation restrictions for the large-span structure or installation space limitations for isolators. In this case, $E_{ds,target}$ and $\sigma_{iso,target}$ are selected as 0.1 and $\sqrt{2}$ (a typical value in Figure 10 for illustration), respectively.

Step 3: Establishment and optimization of design equations

By substituting $E_{ds,target} = 0.1$ and $\sigma_{iso,target} = \sqrt{2}$ into equation (24), the optimization design equations for the IeI are obtained:

$$\begin{cases} \underset{v \in V}{\text{minimize}}, & \xi_{iso}, \\ s.t., & \overline{E_{ds,IeI}} \le 0.1, \overline{\sigma_{iso}} \le \sqrt{2}. \end{cases} \tag{26}$$

Applying numerical methods in MATLAB [64], the solution to equation (26) yields the optimal parameter set $v^{opt} = \{1.265, 0.012, 0.245, 0.253\}$. Consequently, the stiffness κ_{iso}, damping coefficient c_{iso}, and the tuning spring stiffness κ_t are, respectively, 1,264,537 N/m, 6,132 N·s/m, and 305,556 N/m. The apparent masses of the inerter elements, $m_{d,1}$ and $m_{d,2}$, are 4,934 kg.

Step 4: Verification of designed IeI

The time-domain and frequency-domain analyses should be conducted on the large-span structure with

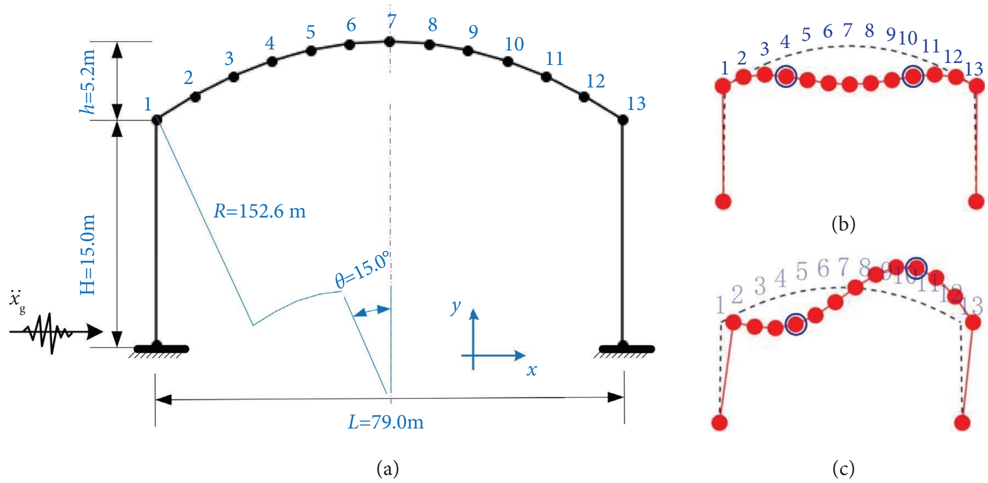

FIGURE 12: Mechanical model of the benchmark structure. (a) Model of the benchmark dome structure. (b) 1st mode (6.76 rad/s). (c) 2nd mode (7.94 rad/s).

IeIs, to verify its compliance with the design requirements. It will be elaborated further in the following section.

4.1. Verification by Frequency-Domain Analysis. Figures 13(a) and 13(b) depict the frequency response functions (FRFs) of the horizontal and vertical displacements relative to the acceleration of ground motions, respectively, at node 4, a representative node of the benchmark structure, as depicted in Figure 12. In Figure 13, $X_4(i\omega)$ and $Y_4(i\omega)$ denote the horizontal and vertical frequency responses of node 4, respectively. $A_g(i\omega)$ represents the Fourier transform of the ground acceleration $\ddot{x}_g(t)$. The FRFs are normalized to the peak FRF value of the uncontrolled structure. Additionally, these figures include the FRF of the benchmark structure with LVD isolators for comparison purposes. The LVD isolator has a stiffness denoted as κ_{iso}, equal to 1,268,900 N/m, and a damping coefficient denoted as c_{iso}, equal to 34,506 N·s/m. It is important to note that the design of the LVD isolator aims to achieve the same design performance indexes, $E_{\text{ds,target}}$ and $\sigma_{\text{iso,target}}$, as the designed IeI, while minimizing the damping cost. It is evident that the second-order mode primarily controls the response of the uncontrolled benchmark structure, with its FRF peak occurring around the frequency of 7.94 rad/s. After the installation of isolation systems, the controlled benchmark structure exhibits a significantly lower frequency at the peak response, which is attributed to the elongation of the vibration period by the isolators.

Additionally, due to the introduction of additional degrees of freedom by the inerter-based damper, the benchmark structure with IeIs exhibits two similar vibration peaks. When using the LVD isolator, the peak values of the horizontal and vertical displacement FRFs at node 4 are 0.545 and 0.444 times those of the uncontrolled structure, respectively. When using the IeI, these peak values are further reduced to 0.444 and 0.356 times those of the uncontrolled structure. It can be determined that the horizontal and vertical RMS displacements at node 4, when isolated by the LVD isolator or the IeI, are roughly 60% and 50% of the uncontrolled ones by comparing the areas under the envelope of the FRFs.

Figure 13(c) shows the energy transfer functions [63, 65, 66], as defined as follows, of the uncontrolled large-span structure and large-span structures with IeIs or LVD isolators:

$$
\begin{aligned}
\mathrm{ETF}_{\mathrm{un}}(\omega) &= \mathrm{Re}\left\{-\frac{i\omega}{\pi}\mathrm{r}^T \mathrm{M}_{\mathrm{p}}^T\left(-\omega^2\mathrm{M}_{\mathrm{p}} + i\omega\mathrm{C}_{\mathrm{p}} + \mathrm{K}_{\mathrm{p}}\right)^{-1}\mathrm{M}_{\mathrm{p}}\mathrm{r}\right\},\\
\mathrm{ETF}_{\mathrm{IeI}}(\omega) &= \mathrm{Re}\left\{-\frac{i\omega}{\pi}r_{\mathrm{c,IeI}}^T \mathrm{M}'^T_{\mathrm{c,IeI}}\left(-\omega^2\mathrm{M}_{\mathrm{c,IeI}} + i\omega\mathrm{C}_{\mathrm{c,IeI}} + \mathrm{K}_{\mathrm{c,IeI}}\right)^{-1}\mathrm{M}_{\mathrm{c,IeI}}{}'r_{\mathrm{c,IeI}}\right\} - \mathrm{Re}\left\{\frac{\omega^2 c_{\mathrm{iso}}}{\pi}\left(\frac{X_{\mathrm{in},1}^2(\omega)}{A_g^2(i\omega)} + \frac{X_{\mathrm{in},2}^2(\omega)}{A_g^2(i\omega)}\right)\right\},\\
\mathrm{ETF}_{\mathrm{LVD}}(\omega) &= \mathrm{Re}\left\{-\frac{i\omega}{\pi}r_{\mathrm{c,LVD}}^T M_{\mathrm{c,LVD}}^T\left(-\omega^2\mathrm{M}_{\mathrm{c,LVD}} + i\omega\mathrm{C}_{\mathrm{c,LVD}} + \mathrm{K}_{\mathrm{c,LVD}}\right)^{-1}\mathrm{M}_{\mathrm{c,LVD}}\mathrm{r}_{\mathrm{c,LVD}}\right\}\\
&\quad - \mathrm{Re}\left\{\frac{\omega^2 c_{\mathrm{iso}}}{\pi}\left(\frac{X_{\mathrm{iso,LVD},1}^2(\omega)}{A_g^2(i\omega)} + \frac{X_{\mathrm{iso,LVD},2}^2(\omega)}{A_g^2(i\omega)}\right)\right\},
\end{aligned}
\tag{27}
$$

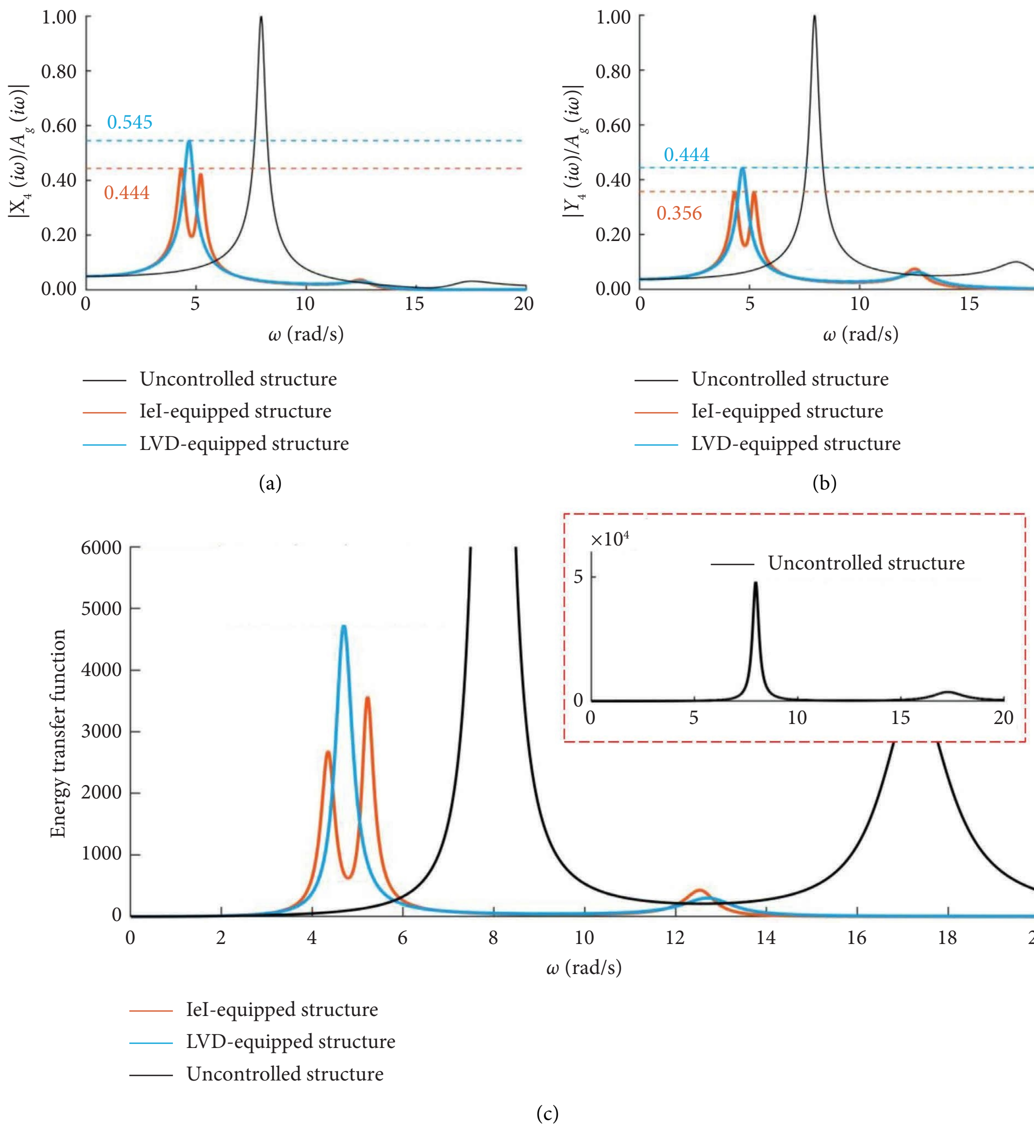

Figure 13: Frequency-domain analysis results of the large-span structures: (a) normalized frequency response functions (FRFs) of x-direction displacement at node 4; (b) normalized FRFs of y-direction displacement at node 4; (c) energy transfer function of the superstructure.

where Re{•} denotes the real part. $X_{\text{in},1}(\omega)$, $X_{\text{in},2}(\omega)$, $X_{\text{iso,LVD},1}(\omega)$, and $X_{\text{iso,LVD},2}(\omega)$ denote the frequency responses of the dashpot displacements within IeIs and LVD isolators, respectively.

The peak value of the uncontrolled structure is observed around the frequency of 7.94 rad/s, reaching 4.80×10^4 kg·m. In contrast, the peak energy transfer function values of the IeI and the LVD isolated structures are 3.57×10^3 kg·m and 4.73×10^3 kg·m, respectively. Despite the smaller peak value, the IeI exhibits a wider energy suppression bandwidth than the LVD isolator. The envelope area under the energy transfer function represents the dissipated energy by the superstructure under unit white noise excitation. For the uncontrolled structure, the envelope area approximates 39,000 kg·m^2/s^2, equal to the total mass of the half-structure, M_0. For the controlled cases, both the IeI and the LVD isolator, the energies dissipated by the superstructures are around 4,200 kg·m^2/s^2. Correspondingly, the IeI and the LVD isolator have similar capabilities in isolating energy transfer, with IeI using only 17.77% of the damping coefficient required by the LVD isolator.

4.2. Verification by Time-Domain Analysis. To further verify the performance of the IeI, time history analyses are performed on uncontrolled and controlled large-span structures using 5 recorded earthquake accelerograms, including the Tohoku earthquake (2011), the Mt. Carmel earthquake (2008), the JMA Kobe earthquake (1995), the El Centro earthquake (1994), and the Hollister earthquake (1961) [67]. For example, Figures 14, 15, 16, and 17 illustrate the time history analysis results of the Tohoku earthquake (2011). The corresponding displacement mitigation ratio γ_{dis}, acceleration mitigation ratio γ_{acc}, shear force ratio γ_{sf}, normalized

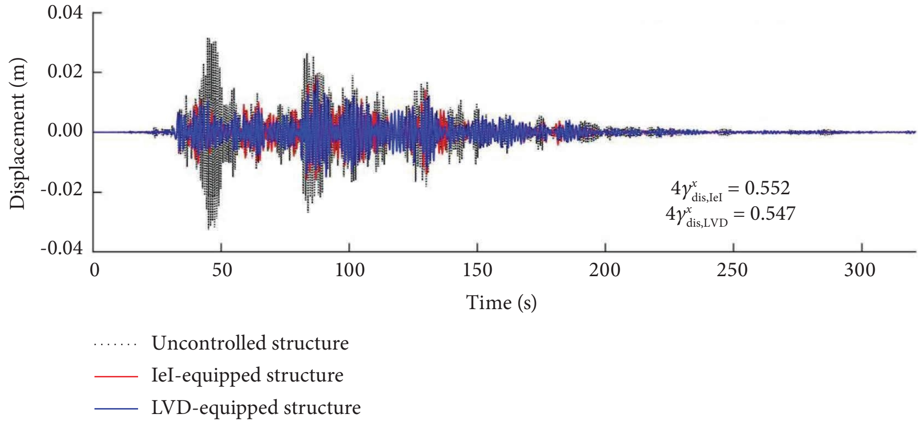

(a)

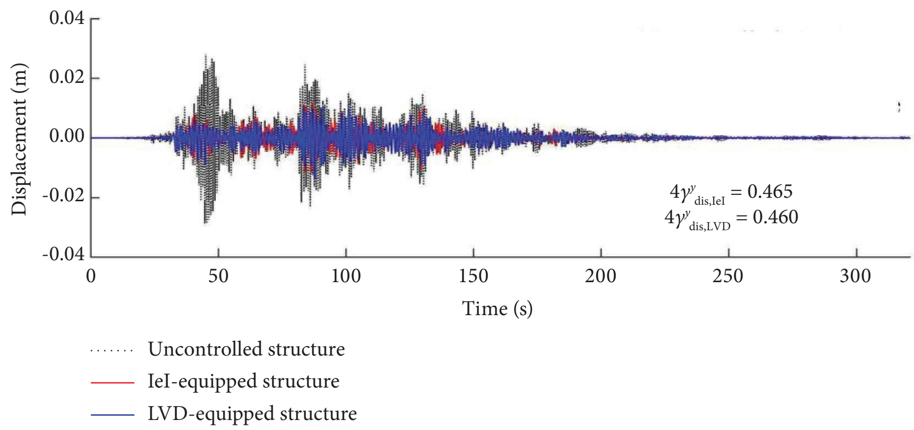

(b)

FIGURE 14: The time history displacement responses of the large-span structures subjected to the Tohoku earthquake (2011). (a) x-direction displacement response of node 4; (b) y-direction displacement response of node 4.

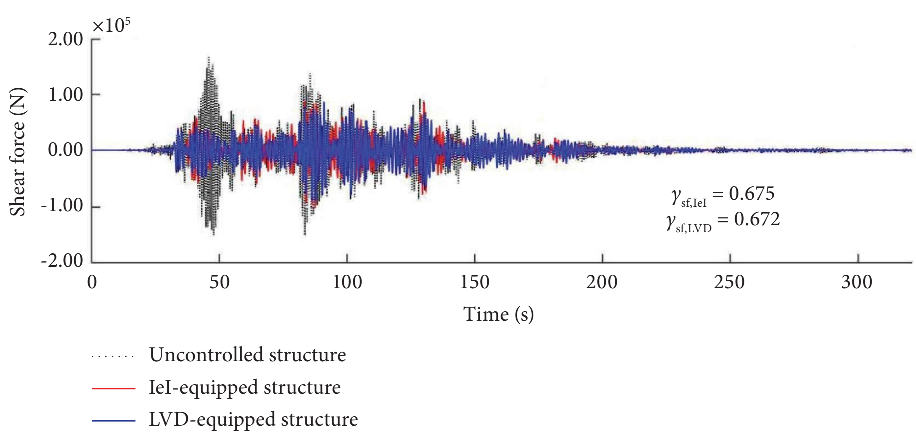

FIGURE 15: The time history base shear force responses of the large-span structures subjected to the Tohoku earthquake (2011).

superstructure energy $\overline{E_{\mathrm{ds}}}$, normalized isolator displacement $\overline{\sigma_{\mathrm{iso}}}$, and damping enhancement ratio γ_{IeI}, defined in the time domain, are marked in the figures. The displacement mitigation ratio γ_{dis} represents the ratio between the RMS displacement of the controlled and uncontrolled large-span structures. Similarly, the acceleration reduction mitigation ratio γ_{acc} is the ratio of the RMS acceleration of the controlled large-span structure to that of the uncontrolled original structure. In contrast, the shear force ratio γ_{sf} is the ratio of the RMS column shear force of the controlled large-span structure to that of the uncontrolled structure. Furthermore, the IeI and the LVD isolator cases are distinguished using the subscript "IeI" and "LVD" in each indicator, e.g., $\gamma_{\mathrm{dis,LVD}}$ and $\gamma_{\mathrm{dis,IeI}}$.

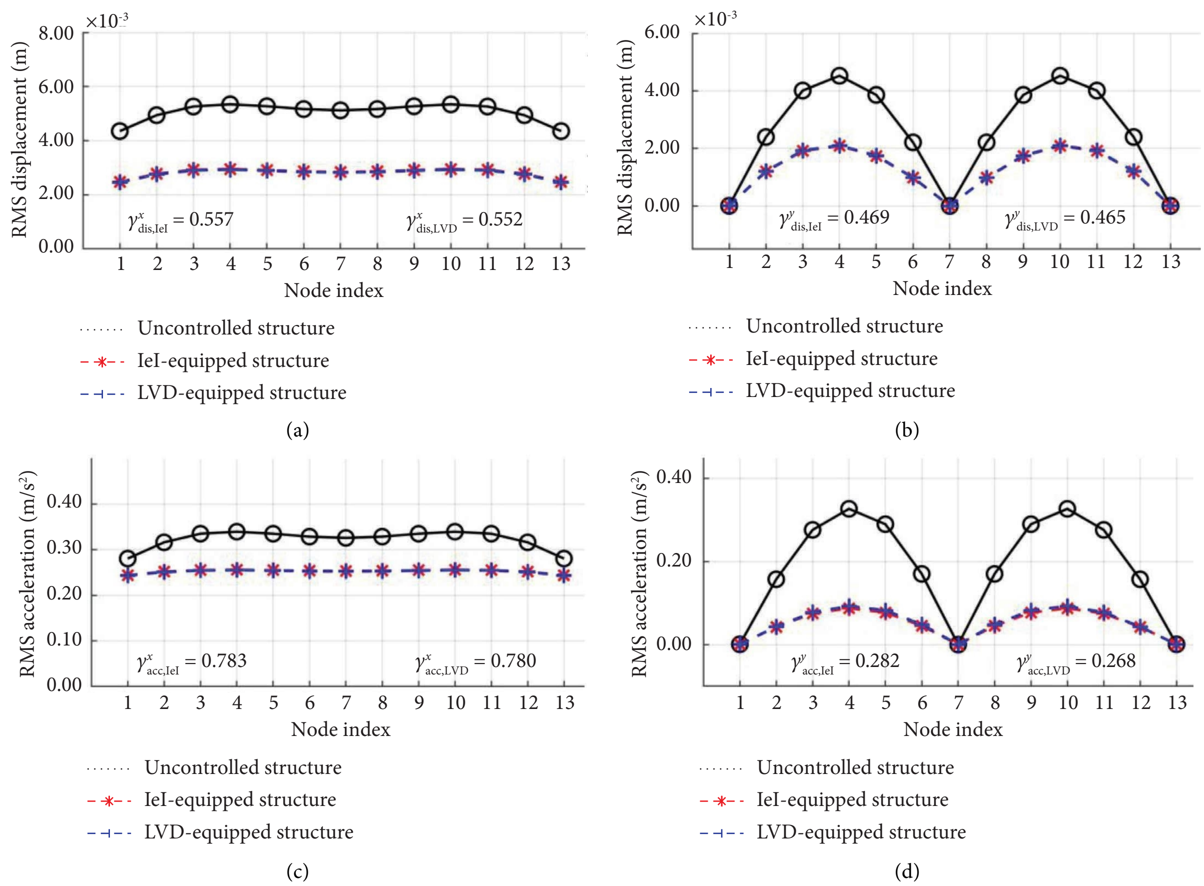

Figure 16: The displacement and acceleration responses of the large-span structure with IeIs or LVD isolators subjected to the Tohoku earthquake (2011): (a) x-direction RMS displacement responses; (b) y-direction RMS displacement responses; (c) x-direction RMS acceleration responses; (d) y-direction RMS acceleration responses.

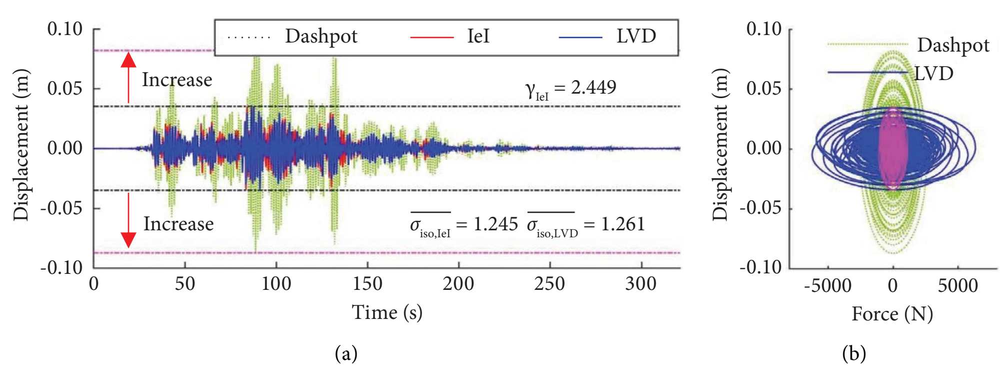

Figure 17: The isolator base and corresponding dashpot displacement of the large-span structure with the IeI and the LVD isolator subjected to the Tohoku earthquake (2011): (a) the time history results; (b) the hysteretic curves.

Table 1: Performance of the large-span structure with IeIs subjected to recorded earthquakes.

Ground motion	$\gamma^x_{\mathrm{dis,IeI}}$	$\gamma^y_{\mathrm{dis,IeI}}$	$\gamma^x_{\mathrm{acc,IeI}}$	$\gamma^y_{\mathrm{acc,IeI}}$	$\gamma_{\mathrm{sf,IeI}}$	γ_{d}	$\overline{\sigma_{\mathrm{iso,IeI}}}$
Tohoku 2011	0.557	0.469	0.783	0.268	0.675	2.450	1.245
Mt. Carmel 2008	0.568	0.464	0.689	0.225	0.711	2.406	1.367
JAM Kobe 1995	0.409	0.360	0.593	0.293	0.475	2.476	0.930
El Centro 1994	0.493	0.419	0.717	0.272	0.589	2.358	1.067
Hollister 1961	0.498	0.417	0.680	0.236	0.597	2.738	1.081
Average	0.505	0.426	0.692	0.259	0.609	2.486	1.138

Table 2: Performance of the large-span structure with LVD isolators subjected to recorded earthquakes.

Ground motion	$\gamma^x_{\text{dis,LVD}}$	$\gamma^y_{\text{dis,LVD}}$	$\gamma^x_{\text{acc,LVD}}$	$\gamma^y_{\text{acc,LVD}}$	$\gamma_{\text{sf,LVD}}$	$\overline{\sigma_{\text{iso,LVD}}}$
Tohoku 2011	0.552	0.465	0.780	0.282	0.672	1.261
Mt. Carmel 2008	0.630	0.516	0.782	0.244	0.786	1.455
JAM Kobe 1995	0.438	0.376	0.617	0.279	0.515	0.985
El Centro 1994	0.444	0.381	0.678	0.280	0.532	1.007
Hollister 1961	0.578	0.479	0.780	0.257	0.697	1.321
Average	0.528	0.443	0.727	0.268	0.640	1.206

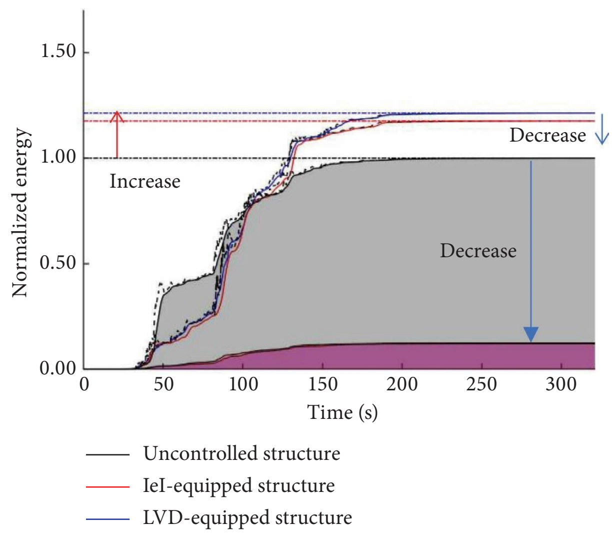

Figure 18: Energy responses of the large-span structure with IeIs or LVD isolators subjected to the Tohoku earthquake (2011).

Table 3: The energy response indexes of the large-span structure with IeIs or LVD isolators subjected to recorded earthquakes.

	Tohoku 2011	Mt. Carmel 2008	Kobe 1995	El Centro 1994	Hollister 1961	Average
$\overline{E_{\text{ds,IeI}}}$	0.123	0.103	0.075	0.101	0.092	0.099
$\overline{E_{\text{damper,IeI}}}$	1.053	1.131	0.424	0.677	0.914	0.840
$\overline{E_{\text{in,IeI}}}$	1.177	1.235	0.499	0.778	1.005	0.939
$\overline{E_{\text{ds,LVD}}}$	0.120	0.131	0.077	0.085	0.116	0.106
$\overline{E_{\text{damper,LVD}}}$	1.094	1.295	0.503	0.655	1.062	0.922
$\overline{E_{\text{in,LVD}}}$	1.214	1.425	0.580	0.740	1.178	1.027
γ_E	0.969	0.866	0.861	1.051	0.854	0.920

Figures 14(a) and 14(b) demonstrate that the displacement mitigation ratios of both the horizontal and vertical responses at typical node 4 are significantly reduced, with a displacement mitigation ratio of approximately 55% and 46%, respectively, due to the isolation of seismic input energy by the IeI and the LVD isolator. Figure 15 illustrates the improved shear-related performance of the controlled large-span structure subjected to real excitation. The performance of the IeI and the LVD isolator is similar, with a shear force ratio of approximately 67%. Furthermore, Figure 16 shows the displacement and acceleration response distributions of controlled and uncontrolled large-span structures. It can be observed that the installation of the IeI or the LVD isolator results in a more uniform response in the x-direction, with an average displacement mitigation ratio of approximately 55%. The y-direction response follows the shape of the second-order uncontrolled mode, as depicted in Figure 10, indicating that the second-order mode dominates the response of both controlled and uncontrolled large-span structures. The average displacement mitigation ratios of the IeI and the LVD isolator are around 47%.

As shown in Figure 17, subjected to the Tohoku earthquake (2011), both the isolator base displacements of the LVD isolator and IeI remain within the target $\sigma_{\text{iso,target}}$, indicating the effectiveness of the proposed design procedure. The damping enhancement ratio, γ_{IeI}, equal to 2.449, indicates a significant amplification of the deformation of the dashpots in the IeI isolator, approximately 2.449 times in terms of RMS. Figure 17(b) presents the hysteresis curves of the dashpot in both the IeI and LVD isolators. Additionally,

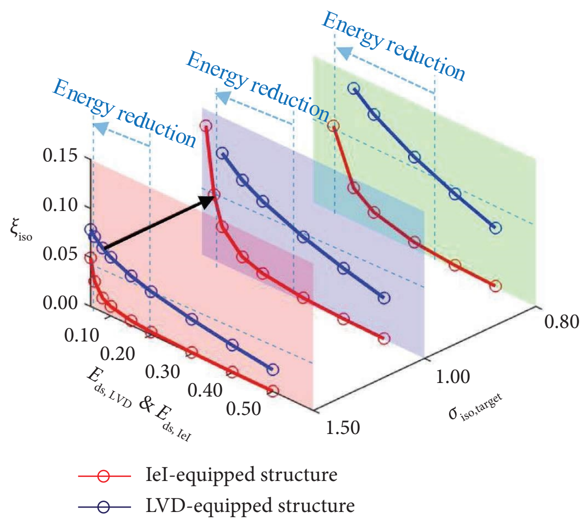

Figure 19: The control effect of IeI and LVD. Transparent green, blue, and red slices correspond to isolator displacement indexes of 0.80, 1.00, and 1.50, respectively.

Table 4: Symbols for the inerter element command in OpenSees.

Symbol	Description	Example
$eleTag	Unique element object tag	3
$iNode	End node number	1
$jNode	End node number	3
$dirs	Material directions	1
$inertance	Value of the apparent mass	25.5

for comparison, the magenta curve represents the hysteresis of the dashpot in the IeI without considering the damping enhancement. It can be observed that the deformation amplification contributes to the improved damping efficiency of the IeI compared with the LVD isolator. Consequently, the IeI requires only 17.77% of the damping coefficient needed by the LVD isolator to achieve comparable energy dissipation effectiveness. Additionally, based on the relevant parameters listed in Tables 1 and 2, we can draw similar conclusions for other recorded earthquake accelerograms consistent with the Tohoku earthquake (2011).

4.3. Discussions on the Energy Responses. In addition to the control performance, some observations related to the energy responses of large-span structures subjected to recorded earthquakes are worth discussing. Figure 18 illustrates the energy responses of controlled and uncontrolled large-span structures subjected to the Tohoku earthquake (2011). Table 3 presents the corresponding energy indexes. In the figure, the black line represents the overall input energy of the uncontrolled original structure. As no additional damping devices are used, all input energy is dissipated by the inherent damping of the uncontrolled structure itself. The red and blue lines represent the overall input energy of the structure with IeIs and the LVD isolators, respectively. Due to the introduction of additional mass by the isolator, the overall input energy of the isolated structure is larger than that of the original structure. However, benefitted from the grounded inerters with optimized distribution, the input energy of the large-span structure with IeI decreases approximately 0.969 times that of the LVD isolator.

Furthermore, Table 3 shows that under the excitation of the Tohoku earthquake (2011), the controlled large-span structure itself dissipates only 12.3% of the energy compared with the uncontrolled original structure, slightly higher than the energy target $E_{ds,target}$. This is primarily due to the significant long-period components of the Tohoku earthquake differing from the unit white noise. On average, the designed IeI and the LVD isolator meet the design target, reducing the energy dissipated by the structure to around 10% of the uncontrolled structure. The overall input energy of the large-span structure controlled by the IeI is approximately 0.920 times that of the LVD isolator, effectively relieving the energy dissipation burden on the entire controlled system subjected to recorded earthquakes.

4.4. Performance Improvement of the IeI. The analysis above demonstrates that, thanks to the reduction in input energy and enhanced damping characteristics, the IeI requires only 17.77% of the damping coefficient used by the LVD isolator to achieve nearly equivalent control performance. To further compare the performance enhancement of IeI over the conventional LVD isolator, Figure 19 illustrates the seismic mitigation effects of both systems on the benchmark large-span structure. This figure considers different target energy dissipation indexes for the superstructure and various isolator displacement indexes, represented by transparent slices indicating the isolator displacement targets. The results consistently show that IeI surpasses the LVD isolator in control performance across all target isolator displacement indexes, resulting in a lower energy dissipation burden on the superstructure. Additionally, as indicated by the black arrow in Figure 19, IeI achieves comparable control performance to the LVD isolator while requiring less isolator displacement.

5. Conclusion

This study has advanced high-efficiency isolation technology for large-span structures by introducing an IeI and developing a design method with analytical design formulae that focus on reducing input energy. The key findings are summarized as follows:

(1) The governing equation analytically established for the IeI has been rigorously validated using finite element simulations and dynamic loading tests to quantify the input energy reduction capacity of the proposed IeI.

(2) Stochastic energy analysis confirms the IeI's effectiveness in significantly reducing the input energy to the large-span structure, assuming the structure remains in the linear stage. By integrating dual inerters, the inertance distribution is optimized, leading to maximal energy reduction. Parametric analysis reveals that equal apparent masses of the inerters (inertance-distribution ratio $\gamma_\mu = 0.5$) result in a substantial decrease in total input energy, outperforming traditional isolation methods.

(3) The input energy reduction-oriented design method achieves an optimized balance between damping performance and isolator displacement. The developed intersection point diagram, illustrating the contour lines of superstructure dissipated energy and isolator displacement for the IeI, proves to be an effective tool for preliminary design in practical engineering applications.

(4) Compared to conventional LVD isolators, the IeI, designed via the energy reduction-oriented method, demonstrates superior seismic mitigation capabilities on a benchmark structure. Both frequency-domain and time-domain analyses validate the significant reduction in input energy and the enhancement in damping provided by the IeI. On average, the IeI reduces input energy by 92% relative to conventional LVD isolators, with a damping enhancement coefficient of 2.486. Moreover, under various isolator displacement constraints, the IeI maintains excellent control performance with reduced isolator displacements. Although this study focuses on horizontal seismic inputs and horizontally installed IeIs, future research will investigate the application of three-dimensional IeI configurations.

Appendix

A. The OpenSees Command for Modeling the Inerter Element

OpenSees Command: element inerter $eleTag $iNode $jNode -dir $dirs -inertance $inertance.

For a detailed description of each parameter used in the command, refer to Table 4, which lists the symbols and their corresponding descriptions and examples.

B. Detailed Derivation of the Energy Index for LVD-Equipped Structures

Given the stiffness k_{iso} and damping coefficient c_{iso} of the LVD isolators, the governing equations for large-span structures with LVD isolators can be expressed as

$$\begin{bmatrix} \mathrm{M_p} & 0 \\ 0 & \mathrm{M_{iso}^{LVD}} \end{bmatrix} \begin{Bmatrix} \ddot{\mathrm{x}}_\mathrm{p} \\ \ddot{\mathrm{y}}_\mathrm{p} \\ \ddot{\theta}_\mathrm{p} \\ \ddot{\mathrm{x}}_\mathrm{iso}^\mathrm{LVD} \end{Bmatrix} + \begin{bmatrix} \mathrm{C_p} & -\mathrm{C_{p,iso}^{LVD^{\mathit{T}}}} \\ -\mathrm{C_{p,iso}^{LVD}}, & \mathrm{C_{iso}^{LVD}} \end{bmatrix} \begin{Bmatrix} \dot{\mathrm{x}}_\mathrm{p} \\ \dot{\mathrm{y}}_\mathrm{p} \\ \dot{\theta}_\mathrm{p} \\ \dot{\mathrm{x}}_\mathrm{iso}^\mathrm{LVD} \end{Bmatrix} + \begin{bmatrix} \mathrm{K_p} & -\mathrm{K_{p,iso}^{LVD^{\mathit{T}}}} \\ -\mathrm{K_{p,iso}^{LVD}}, & \mathrm{K_{iso}^{LVD}} \end{bmatrix} \begin{Bmatrix} \mathrm{x}_\mathrm{p} \\ \mathrm{y}_\mathrm{p} \\ \theta_\mathrm{p} \\ \mathrm{x}_\mathrm{iso}^\mathrm{LVD} \end{Bmatrix} = -\begin{bmatrix} \mathrm{M_p} & 0 \\ 0 & \mathrm{M_{iso}^{LVD}} \end{bmatrix} \begin{Bmatrix} \mathrm{r} \\ 1_{2\times 1} \end{Bmatrix} \ddot{x}_\mathrm{g}, \tag{B.1}$$

where

$$\begin{aligned}
\mathrm{M}_{\text{iso}}^{\text{LVD}} &= \begin{bmatrix} m_{\text{iso}} & 0 \\ 0 & m_{\text{iso}} \end{bmatrix}, \\
\mathrm{K}_{\text{iso}}^{\text{LVD}} &= \begin{bmatrix} k_{\text{iso}} + k_{\text{x}}^{\text{column}} & 0 \\ 0 & k_{\text{iso}} + k_{\text{x}}^{\text{column}} \end{bmatrix}, \\
\mathrm{C}_{\text{iso}}^{\text{LVD}} &= \begin{bmatrix} c_{\text{iso}} + \alpha_{\text{p}} k_{\text{x}}^{\text{column}} & 0 \\ 0 & c_{\text{iso}} + \alpha_{\text{p}} k_{\text{x}}^{\text{column}} \end{bmatrix}, \\
\mathrm{K}_{\text{p,iso}}^{\text{LVD}} &= \begin{bmatrix} k_{\text{x}}^{\text{column}} & 0_{2n_{\text{p}}-1} & k_{\theta}^{\text{column}} & 0_{n_{\text{p}}-1} \\ 0_{n_{\text{p}}-1} & k_{\text{x}}^{\text{column}} & 0_{2n_{\text{p}}-1} & k_{\theta}^{\text{column}} \end{bmatrix}, \\
\mathrm{C}_{\text{p,iso}}^{\text{LVD}} &= \alpha_{\text{p}} \mathrm{K}_{\text{iso}}, \\
\mathrm{x}_{\text{iso}}^{\text{LVD}} &= \left[x_{\text{iso,LVD,1}} \ \ x_{\text{iso,LVD,2}} \right]^{T}.
\end{aligned} \tag{B.2}$$

By applying static condensation [60], equation (B.1) can be expressed as

$$\begin{aligned}
&\mathrm{M}_{\text{c,LVD}} \ddot{\mathrm{X}}_{\text{c,LVD}} + \mathrm{C}_{\text{c,LVD}} \dot{\mathrm{X}}_{\text{c,LVD}} + \mathrm{K}_{\text{c,LVD}} \mathrm{X}_{\text{c,LVD}} \\
&\quad = -\mathrm{M}_{\text{c,LVD}} \mathrm{r}_{\text{c,LVD}} \ddot{x}_{\text{g}},
\end{aligned} \tag{B.3}$$

where

$$\begin{aligned}
\mathrm{M}_{\text{c,LVD}} &= \begin{bmatrix} \mathrm{M}_{\text{p,x}} & 0 & 0 \\ 0 & \mathrm{M}_{\text{p,y}} & 0 \\ 0 & 0 & \mathrm{M}_{\text{iso}}^{\text{LVD}} \end{bmatrix}, \\
\mathrm{X}_{\text{c,LVD}} &= \begin{Bmatrix} \mathrm{x}_{\text{p}} \\ \mathrm{y}_{\text{p}} \\ \mathrm{x}_{\text{iso}}^{\text{LVD}} \end{Bmatrix}, \\
\mathrm{K}_{\text{c,LVD}} &= \mathrm{K}_{\text{T}}^{\text{LVD}} - \mathrm{K}_{\text{T}\theta}^{\text{LVD}} K_{\theta}^{\text{LVD}^{-1}} C_{\text{T}\theta}^{\text{LVD}^{T}}, \\
\mathrm{C}_{\text{c,LVD}} &= \mathrm{C}_{\text{T}}^{\text{LVD}} - \mathrm{C}_{\text{T}\theta}^{\text{LVD}} C_{\theta}^{\text{LVD}^{-1}} C_{\text{T}\theta}^{\text{LVD}^{T}},
\end{aligned} \tag{B.4}$$

where $\mathrm{K}_{\text{T}}^{\text{LVD}}$, $\mathrm{K}_{\text{T}\theta}^{\text{LVD}}$, $\mathrm{K}_{\theta}^{\text{LVD}}$, $\mathrm{C}_{\text{T}}^{\text{LVD}}$, $\mathrm{C}_{\text{T}\theta}^{\text{LVD}}$, and $\mathrm{C}_{\theta}^{\text{LVD}}$ are obtained by reorganizing the stiffness and damping matrix in equation (B.1) based on translational displacements and rotations. The vector $r_{\text{c,LVD}}$ represents the influence vector considering the isolation layer.

Therefore, these equations can be represented in state-space form as

$$\dot{\mathrm{X}}_{\text{s,LVD}}(t) = \mathrm{A}_{\text{s,LVD}} \mathrm{X}_{\text{s,LVD}}(t) + \mathrm{E}_{\text{s,LVD}} w(t), \tag{B.5}$$

where

$$\begin{aligned}
\mathrm{X}_{\text{s,LVD}}(t) &= \begin{bmatrix} \mathrm{X}_{\text{c,LVD}} \\ \dot{\mathrm{X}}_{\text{c,LVD}} \end{bmatrix}, \\
\mathrm{A}_{\text{s,LVD}} &= \begin{bmatrix} 0 & \mathrm{I} \\ -\mathrm{M}_{\text{c,LVD}}{}^{-1} \mathrm{K}_{\text{c,LVD}}, & -\mathrm{M}_{\text{c,LVD}}{}^{-1} \mathrm{C}_{\text{c,LVD}}, \end{bmatrix}, \\
\mathrm{E}_{\text{s,LVD}} &= \begin{bmatrix} 0 \\ \mathrm{r}_{\text{c,LVD}} \end{bmatrix}.
\end{aligned} \tag{B.6}$$

Thus, the overall input energy and the energy dissipated by the dashpot and superstructure of the large-span structures with LVD isolators, namely, $E_{\text{in,LVD}}$, $E_{\text{damper,LVD}}$, and $E_{\text{ds,LVD}}$, can be derived as follows:

$$\begin{aligned}
E_{\text{in,LVD}} &= \tau_{\text{LVD}}{}^{T} \left(C_{c,\text{LVD}} .* \sum_{\dot{X}_{c,\text{LVD}} \dot{X}_{c,\text{LVD}}} \right) \tau_{\text{LVD}}, \\
E_{\text{damper,LVD}} &= \int_0^{\infty} \dot{\mathrm{x}}_{\text{iso,LVD,1}} \mathrm{c}_{\text{iso}} \dot{\mathrm{x}}_{\text{iso,LVD,1}}^{\mathrm{T}} dt + \int_0^{\infty} \dot{\mathrm{x}}_{\text{iso,LVD,2}}^{\mathrm{T}} \mathrm{c}_{\text{iso}} \dot{x}_{\text{iso,LVD,2}}^{T} dt = c_{\text{iso}} \left(\sigma_{\dot{x}_{\text{iso,LVD,1}}}^2 + \sigma_{\dot{x}_{\text{iso,LVD,2}}}^2 \right), \\
E_{\text{ds,LVD}} &= E_{d,\text{LVD}} - E_{\text{damper,LVD}},
\end{aligned} \tag{B.7}$$

where τ_{LVD} is an $n_{\text{p}}+2$ column unit vector; $\Sigma_{\dot{X}_{\text{c,LVD}} \dot{X}_{\text{c,LVD}}}$ denotes the covariance matrix of the velocity responses of the large-span structure with LVD isolators. $\sigma_{\dot{x}_{\text{iso,LVD,1}}}$ and $\sigma_{\dot{x}_{\text{iso,LVD,2}}}$ denote the root-mean-square velocity responses of the two LVD isolation layers. These can be obtained from the state covariance matrix $P_{\text{s,LVD}}$, which is obtained by solving the following Lyapunov equation:

$$\mathrm{A}_{\text{s,LVD}} \mathrm{P}_{\text{s,LVD}} + \mathrm{P}_{\text{s,LVD}}^{T} \mathrm{A}_{\text{s,LVD}} + \mathrm{E}_{\text{s,LVD}} \mathrm{E}_{\text{s,LVD}}^{T} = 0. \tag{B.8}$$

Data Availability

The data that support the findings of this study are available from the corresponding author upon reasonable request.

Conflicts of Interest

The authors declare that they have no known conflicts of financial interest or personal relationships that could have appeared to influence the work reported in this paper.

Acknowledgments

This study was supported by the National Natural Science Foundation of China (grant no. 52308525), the National Key R&D Program of China (grant no. 2021YFE0112200), the Natural Science Foundation of Shanghai (grant no. 20ZR1461800), and the Fundamental Research Funds for the Central Universities (grant no. 22120240428 and grant no. 2023-2-YB-05). All support is gratefully acknowledged.

References

[1] R. Bradshaw, D. Campbell, M. Gargari, A. Mirmiran, and P. Tripeny, "Special structures: past, present, and future," *Journal of Structural Engineering*, vol. 128, no. 6, pp. 691–709, 2002.

[2] H. Nakamura, *Preliminary Report on the Great Hanshin Earthquake January 17, 1995*, Japan Society of Civil Engineers, Tokyo, Japan, 1995.

[3] K. Kawaguchi, "A report on large roof structures damaged by the great Hanshin-Awaji earthquake," *International Journal of Space Structures*, vol. 12, no. 3–4, pp. 135–147, 1997.

[4] Y. Feng, Y. Liu, and K. Xiao, *Experience the Wenchuan Earthquake—Structural Engineers' Point and View*, China Architecture and Building Press, Beijing, China, 2009.

[5] N. Mimura, K. Yasuhara, S. Kawagoe, H. Yokoki, and S. Kazama, "Damage from the great east Japan earthquake and tsunami—a quick report," *Mitigation and Adaptation Strategies for Global Change*, vol. 16, no. 7, pp. 803–818, 2011.

[6] J. Dai, Z. Qu, C. Zhang, and X. Weng, "Preliminary investigation of seismic damage to two steel space structures during the 2013 lushan earthquake," *Earthquake Engineering and Engineering Vibration*, vol. 12, no. 3, pp. 497–500, 2013.

[7] H. Li, L. Zhao, R. Huang, and Q. Hu, "Hierarchical earthquake shelter planning in urban areas: a case for shanghai in China," *International Journal of Disaster Risk Reduction*, vol. 22, pp. 431–446, 2017.

[8] A. Feizolahbeigi, P. B. Lourenço, M. Golabchi, J. Ortega, and M. Rezazadeh, "Discussion of the role of geometry, proportion and construction techniques in the seismic behavior of 16th to 18th century bulbous discontinuous double shell domes in central Iran," *Journal of Building Engineering*, vol. 33, Article ID 101575, 2021.

[9] L. Tian, D. Li, W. Li, and Y. Kou, "Progressive collapse resistance of single-layer latticed domes under different failure conditions at the same joint," *Journal of Building Engineering*, vol. 36, Article ID 102132, 2021.

[10] E. Mrabet, M. H. El Ouni, and N. Ben Kahla, "Robust multimodal control of a large-scale tensegrity dome using multiple tuned mass dampers," *Structural Control and Health Monitoring*, vol. 28, no. 11, Article ID e2815, 2021.

[11] K. Ishikawa and S. Kato, "Elastic-plastic dynamic buckling analysis of reticular domes Subjected to Earthquake Motion," *International Journal of Space Structures*, vol. 12, no. 3–4, pp. 205–215, 1997.

[12] S. Kato, T. Ueki, and Y. Mukaiyama, "Study of dynamic collapse of single layer reticular domes subjected to earthquake motion and the estimation of statically equivalent seismic forces," *International Journal of Space Structures*, vol. 12, no. 3–4, pp. 191–203, 1997.

[13] T. Takeuchi, T. Ogawa, and T. Kumagai, "Seismic response evaluation of lattice shell roofs using amplification factors," *Journal of the International Association for Shell and Spatial Structures*, vol. 48, no. 3, pp. 197–210, 2007.

[14] G. Nie, X. Zhi, F. Fan, and J. Dai, "Failure pattern of singe-layer reticulated dome under severe earthquake and its shaking table test," *International Journal of Steel Structures*, vol. 14, no. 2, pp. 399–409, 2014.

[15] G. Nie, C. Zhang, X. Zhi, and J. Dai, "Collapse of the single layered cylinder shell with model experimental study," *Archives of Civil and Mechanical Engineering*, vol. 19, no. 3, pp. 883–897, 2019.

[16] G. Nie, C. X. Zhang, D. f. Li, Q. Chen, and Z. Wang, "Collapse of the spatial double-layer cylinder shell by experimental study," *Engineering Structures*, vol. 245, Article ID 112862, 2021.

[17] F. Fan, S. Z. Shen, and G. A. R. Parke, "Theoretical and experimental study of vibration reduction in braced domes using a viscous damper system," *International Journal of Space Structures*, vol. 19, no. 4, pp. 195–202, 2004.

[18] S. Kato, Y. Takiuchi, K. Abe, Y. Mukaiyama, and S. Nakazawa, "Effectiveness of buckling restrained braces for upgrading earthquake resistant capacity of single layer grid dome," *Engineering Structures*, vol. 261, Article ID 114280, 2022.

[19] S. Tsuda and M. Ohsaki, "Parameter optimization of mass damper consisting of compliant mechanism for bi-directional control of spatial structures," *Journal of Structural and Construction Engineering (Transactions of AIJ)*, vol. 77, no. 673, pp. 379–387, 2012.

[20] J. Kang, L. Xie, S. Xue, and Z. Zhao, "Simplified optimization of inerter-enabled tuned mass damper for lightweight-oriented seismic response mitigation of long-span domes," *Structures*, vol. 58, Article ID 105408, 2023.

[21] N. Güneş, A. Giaralis, and N. Güneş, "Risk-targeted design of seismically isolated buildings," *Journal of Building Engineering*, vol. 46, Article ID 103665, 2022.

[22] X. Zhi, N. Liang, L. Yin, and F. Fan, "Mechanical properties of curvature-consistent frictional pendulum bearings and isolation performance of spherical reticulated shells," *Journal of Building Engineering*, vol. 64, Article ID 105659, 2023.

[23] Y. C. Kim, J. W. Hu, X. Zhi, N. Liang, L. Yin, and F. Fan, "Experimental performance verification of rubber friction bearing," *Journal of Building Engineering*, vol. 75, Article ID 107001, 2023.

[24] W. Zheng, P. Tan, J. Li, H. Wang, Y. Liu, and Z. Xian, "Superelastic pendulum isolator with multi-stage variable curvature for seismic resilience enhancement of cold-regional bridges," *Engineering Structures*, vol. 284, Article ID 115960, 2023.

[25] T. Li, Y. Yang, K. Dai, Q. Ge, and J. Wang, "Influence of ground motion duration on seismic performance of RC frame isolated by high damping rubber bearings," *Engineering Structures*, vol. 262, Article ID 114398, 2022.

[26] K. Yong-Chul, S. Xue, P. Zhuang, W. Zhao, and C. Li, "Seismic isolation analysis of FPS bearings in spatial lattice shell structures," *Earthquake Engineering and Engineering Vibration*, vol. 9, no. 1, pp. 93–102, 2010.

[27] Q. Han, M. Jing, Y. Lu, and M. Liu, "Mechanical behaviors of air spring-FPS three-dimensional isolation bearing and isolation performance analysis," *Soil Dynamics and Earthquake Engineering*, vol. 149, Article ID 106872, 2021.

[28] Z. Xu, T. Zhang, and X. Huang, "Dynamic analysis of three-directional vibration isolation and mitigation for long-span grid structure," *Journal of Constructional Steel Research*, vol. 202, Article ID 107758, 2023.

[29] S. Casciati, "Comparing the efficiency of different structural skeleton for base isolated domes," *Bulletin of the Polish Academy of Sciences, Technical Sciences*, vol. 1, Article ID e143555, 2022.

[30] H. Sun, L. Zuo, X. Wang, J. Peng, and W. Wang, "Exact H_2 optimal solutions to inerter-based isolation systems for building structures," *Structural Control and Health Monitoring*, vol. 26, no. 6, Article ID e2357, 2019.

[31] C. Pan, J. Jiang, R. Zhang, and Y. Xia, "Closed-form design formulae for seismically isolated structure with a damping enhanced inerter system," *Structural Control and Health Monitoring*, vol. 28, no. 12, Article ID e2840, 2021.

[32] B. Chen, Z. Zhang, and X. Hua, "Equal modal damping-based optimal design of a grounded tuned mass-damper-inerter for flexible structures," *Structural Control and Health Monitoring*, vol. 29, no. 12, Article ID e3106, 2022.

[33] S. Kawamata, "Accelerated liquid mass damper and principles of structural vibration control," in *Proceedings of the Transactions of the International Conference on Structural Mechanics in Reactor Technology*, pp. 737–742, Lausanne, Switzerland, June 1987.

[34] M. C. Smith, "Synthesis of mechanical networks: the inerter," *IEEE Transactions on Automatic Control*, vol. 47, no. 10, pp. 1648–1662, 2002.

[35] T. Arakaki, H. Kuroda, F. Arima, Y. Inoue, and K. Baba, "Development of seismic devices applied to ball screw: part 1 basic performance test of RD-series," *AIJ Journal of Technology and Design*, vol. 5, no. 8, pp. 239–244, 1999.

[36] T. Arakaki, H. Kuroda, F. Arima, Y. Inoue, and K. Baba, "Development of seismic devices applied to ball screw: part 2 performance test and evaluation of RD-series," *AIJ Journal of Technology and Design*, vol. 5, no. 9, pp. 265–270, 1999.

[37] F. C. Wang, M. F. Hong, and T. C. Lin, "Designing and testing a hydraulic inerter," *Proceedings of the Institution of Mechanical Engineers-Part C: Journal of Mechanical Engineering Science*, vol. 225, no. 1, pp. 66–72, 2011.

[38] L. Xie, X. Ban, S. Xue, K. Ikago, J. Kang, and H. Tang, "Theoretical study on a cable-bracing inerter system for seismic mitigation," *Applied Sciences*, vol. 9, no. 19, p. 4096, 2019.

[39] Z. Zhao, R. Zhang, Y. Jiang, and C. Pan, "A tuned liquid inerter system for vibration control," *International Journal of Mechanical Sciences*, vol. 164, Article ID 105171, 2019.

[40] R. Ma, K. Bi, and H. Hao, "Inerter-based structural vibration control: a state-of-the-art review," *Engineering Structures*, vol. 243, Article ID 112655, 2021.

[41] C. Liu, L. Chen, H. P. Lee, Y. Yang, and X. Zhang, "A review of the inerter and inerter-based vibration isolation: theory, devices, and applications," *Journal of the Franklin Institute*, vol. 359, no. 14, pp. 7677–7707, 2022.

[42] K. Ikago, K. Saito, and N. Inoue, "Seismic control of single-degree-of-freedom structure using tuned viscous mass damper," *Earthquake Engineering and Structural Dynamics*, vol. 41, no. 3, pp. 453–474, 2012.

[43] I. F. Lazar, S. A. Neild, and D. J. Wagg, "Using an inerter-based device for structural vibration suppression," *Earthquake Engineering and Structural Dynamics*, vol. 43, no. 8, pp. 1129–1147, 2014.

[44] A. Giaralis and A. A. Taflanidis, "Optimal tuned mass-damper-inerter (TMDI) design for seismically excited MDOF structures with model uncertainties based on reliability criteria," *Structural Control and Health Monitoring*, vol. 25, no. 2, Article ID e2082, 2018.

[45] A. Kaveh, M. Fahimi Farzam, and H. Hojat Jalali, "Statistical seismic performance assessment of tuned mass damper inerter," *Structural Control and Health Monitoring*, vol. 27, no. 10, Article ID e2602, 2020.

[46] H. Hojat Jalali and M. Fahimi Farzam, "Inerter-connected double tuned mass damper for passive control of buildings under seismic excitation," *Periodica Polytechnica: Civil Engineering*, vol. 66, no. 2, pp. 421–432, 2022.

[47] X. Yang, Y. Lei, L. Liu, H. Zhu, and W. Shen, "Two-step online identification of in-service cable-inertial mass damper systems under nonstationary wind excitations," *Mechanical Systems and Signal Processing*, vol. 187, Article ID 109940, 2023.

[48] T. Konar and A. D. Ghosh, "Tuned mass damper inerter for seismic control of multi-story buildings: ten years since inception," *Structures*, vol. 63, Article ID 106459, 2024.

[49] R. Zhang, Z. Zhao, C. Pan, K. Ikago, and S. Xue, "Damping enhancement principle of inerter system," *Structural Control and Health Monitoring*, vol. 27, no. 5, Article ID e2523, 2020.

[50] J. Kang, S. Xue, L. Xie, H. Tang, and R. Zhang, "Multi-modal seismic control design for multi-storey buildings using cross-layer installed cable-bracing inerter systems: part 1 theoretical treatment," *Soil Dynamics and Earthquake Engineering*, vol. 164, Article ID 107639, 2023.

[51] Z. Zhao, Q. Chen, R. Zhang, C. Pan, and Y. Jiang, "Energy dissipation mechanism of inerter systems," *International Journal of Mechanical Sciences*, vol. 184, Article ID 105845, 2020.

[52] S. Nakaminami, K. Ikago, N. Inoue, and H. Kida, "Response characteristics of a base-isolated structure incorporated with a force-restricted viscous mass damper," in *Proceedings of the 15th world conference on earthquake engineering*, Lisbon, Portugal, May 2012.

[53] D. De Domenico and G. Ricciardi, "An enhanced base isolation system equipped with optimal tuned mass damper inerter (TMDI)," *Earthquake Engineering and Structural Dynamics*, vol. 47, no. 5, pp. 1169–1192, 2018.

[54] D. De Domenico, G. Ricciardi, and R. Zhang, "Optimal design and seismic performance of tuned fluid inerter applied to structures with friction pendulum isolators," *Soil Dynamics and Earthquake Engineering*, vol. 132, Article ID 106099, 2020.

[55] Z. Zhao, R. Zhang, N. E. Wierschem, Y. Jiang, and C. Pan, "Displacement mitigation–oriented design and mechanism for inerter-based isolation system," *Journal of Vibration and Control*, vol. 27, no. 17–18, pp. 1991–2003, 2021.

[56] W. M. Kuhnert, P. J. P. Gonçalves, D. F. Ledezma-Ramirez, and M. J. Brennan, "Inerter-like devices used for vibration isolation: a historical perspective," *Journal of the Franklin Institute*, vol. 358, no. 1, pp. 1070–1086, 2021.

[57] Y. Lei and X. Yang, "Stochastic optimization of electromagnetic inertial mass dampers in nonlinear hybrid base isolation systems under seismic excitations," *International Journal of Structural Stability and Dynamics*, vol. 1, Article ID 2450241, 2023.

[58] Y. Tai, Z. Huang, C. Chen, X. Hua, and Z. Chen, "Geometrically nonlinearity analysis and performance evaluation of tuned inerter dampers for multidirectional seismic isolation," *Mechanical Systems and Signal Processing*, vol. 168, Article ID 108681, 2022.

[59] K. L. Ryan and J. Polanco, "Problems with Rayleigh damping in base-isolated buildings," *Journal of Structural Engineering*, vol. 134, no. 11, pp. 1780–1784, 2008.

[60] A. K. Chopra, *Dynamics of Structures*, Pearson Education Limited, Upper Saddle River, NJ, USA, 2019.

[61] L. D. Lutes and S. Sarkani, *Random Vibrations: Analysis of Structural and Mechanical Systems*, Butterworth-Heinemann, Oxford, UK, 2003.

[62] D. De Domenico and G. Ricciardi, "Earthquake protection of structures with nonlinear viscous dampers optimized through an energy-based stochastic approach," *Engineering Structures*, vol. 179, pp. 523–539, 2019.

[63] I. Takewaki, "Frequency domain modal analysis of earthquake input energy to highly damped passive control structures," *Earthquake Engineering and Structural Dynamics*, vol. 33, no. 5, pp. 575–590, 2004.

[64] The MathWorks Inc, *Optimization Toolbox Version: 9.4 (R2022b)*, The MathWorks Inc, Natick, MA, USA, 2022.

[65] Z. Zhao, R. Zhang, C. Pan, Q. Chen, and Y. Jiang, "Input energy reduction principle of structures with generic tuned mass damper inerter," *Structural Control and Health Monitoring*, vol. 28, no. 1, 2021.

[66] Z. Zhao, X. Hu, R. Zhang, M. Xie, and S. Liu, "Advantages and design of inerters for isolated storage tanks incorporating soil conditions," *Thin-Walled Structures*, vol. 195, Article ID 111356, 2024.

[67] C. A. Goulet, T. Kishida, T. D. Ancheta et al., "PEER NGA-east database," *Earthquake Spectra*, vol. 37, no. 1_suppl, pp. 1331–1353, 2021.